

https://dspace.org/

Ab-initio Study of the Properties of Advanced Metal Nitrides

Orisakwe, Esther Nkiruka

2011-10-12
http://hdl.handle.net/10539/10539

Downloaded from a DSpace repository. https://dspace.org/

Ab-initio Study of the Properties of Advanced Metal Nitrides

Esther Nkiruka Orisakwe

DST/NRF Centre of Excellence in Strong Materials and School of Physics.

University of the Witwatersrand, Johannesburg.

A dissertation submitted to the Faculty of Science,

University of Witwatersrand (WITS), Johannesburg,

In fulfilment of the requirements for the degree of Master of Science.

July 1, 2011

Declaration

I, the undersigned, hereby declare that this dissertation is my own work. It is being submitted for the degree of Master of Science in the University of the Witwatersrand, Johannesburg. It has not been submitted before for any degree or examination in any other University.

Esther Nkiruka Orisakwe

(Signature of Candidate)

on the_____ of_____ 2011.

Dedication

My greatest debt is to God Almighty for His outrageous grace upon my life.

!!!! Emela Chineke, emela onyewem. Ihi ne eme jurum anya. !!!!

Abstract

Materials are modeled by the ab-initio plane wave pseudopotential methods using density functional theory. In this work, we are seeking new ultrahard with enhanced elastic and mechanical properties, thermal stability as well as hardness which might be of advantage over known traditional materials (diamond and cubic boron nitride). Structural, elastic and electronic properties of the advanced metal nitrides M_2N_3 and their ternary phases were investigated using both the local density approximation (LDA) and the generalized gradient approximation (GGA). The relative stability of the ternary phases with respect to their constituent mixtures is computed. Results obtained are compared with the available experimental and theoretical data. To gain more information concerning the elastic properties of these hypothetical materials, we also computed the charge densities of the binary and ternary phases. From these calculations suggestions are made as to how the elastic properties vary from those of known hard materials.

Acknowledgements

I wish to express my profound gratitude to my supervisor Prof. J.E. Lowther for his encouragement and support throughout the preparation of this project. He has influenced my thinking about the subject in ways too numerous to list.

Special thanks to Dr. Vinit Sharma for his immense contribution. To my family members, for standing with me in prayers, I say thank you.

To my friends and colleague in the School of Physics, no names mentioned, many thanks to all of you.

Finally, I want to acknowledge all the financial support received from DST/NRF Centre of Excellence in Strong Materials and the University of Witwatersrand.

Contents

Declaration i

Dedication ii

Abstract iii

Acknowledgements iv

List of Figures x

List of Tables x

1 Introduction 1

2 Overview of Ultrahard Materials 5

2.1 Concept of Hardness 9

3 Theoretical Background 14

3.1 Density Functional Theory (DFT) 15

3.2 Hohenberg-Kohn Theorems 16

3.3 Kohn-Sham Approach to Density Functional Theorem 19

3.4 Local Density Approximation (LDA) 21

3.5 Generalized Gradient Approximation (GGA) 24

3.6 Plane Wave Approach of Density Functional Theory 25

3.7 Pseudopotentials 29

3.8 Vienna Ab-initio Simulation Package 34

4 The Transition Metal Nitrides **35**

4.1 Tantalum Nitrides 37

5 Elastic, Structural, Electronic and Relative Stability Properties of the Orthorhombic Metal Nitrides of Tantalum, Vanadium and Niobium **39**

5.1 Elasticity of the Orthorhombic Metal nitride 39

5.2 Calculation of the Isotropic Moduli 41

5.3 The Equation of State 42

5.4 Results Analysis 44

5.4.1 Computational Analysis 44

5.4.2 Cell Parameters of the Metal Nitrides 45

5.4.3 Structural Properties Calculation 51

5.4.4 Calculated Elastic Properties 53

5.4.5 Relative Stability 60

5.5 Electronic Structure Calculation 63

6 Conclusion **76**

6.1 Direction for Future Work 78

References **78**

List of Figures

3.1 The schematic illustration of the pseudoelectron (dashed lines) and the all-electron (solid lines) potentials and their corresponding wavefunctions. $\mathbf{R_c}$ is the radius at which the all-electron and pseudoelectron value match. 32

5.1 Crystal structures of the binary metal nitrides with U_2S_3 structure. 49

5.2 Crystal structures of the ternary metal nitrides with U_2S_3 structure. 50

5.3 The isotropic bulk properties (LDA and the GGA values) of the binary metal nitrides and their ternary phases at plane wave energy cutoff of 500eV. . . . 59

5.4 The relative stability (LDA and GGA values) of the ternary phases of the metal nitrides in $Ta-V-N$ and $Nb-Ta-N$ trends at energy cutoff 400eV. 61

5.5 The relative stability (LDA and GGA values) of the ternary phases of the metal nitrides in $Ta-V-N$ and $Nb-Ta-N$ trends at energy cutoff 500eV. 62

5.6 The Brillouin zone of the orthorhombic unit cell with points of high symmetry indicated. 64

5.7 Electronic band structure for Ta_2N_3 using both VASP and WIEN2K (at the bottom). The Fermi energy level is set at 0 eV. 66

5.8 Electronic band structure for V_2N_3 using both VASP and WIEN2K (at the bottom). The Fermi energy level is set at 0 eV. 67

5.9 Calculated electronic band structure for Nb_2N_3 using VASP. The Fermi energy level is set at 0 eV. 68

5.10 Electronic band structure for the ternary metal nitrides. The Fermi energy level is set at 0 eV. 69

5.11 Electronic band structure for the ternary metal nitrides. The Fermi energy level is set at 0 eV. (The WIEN2K results at the bottom). 70

5.12 The plots of the total density of states (DOS) of the binary metal nitrides. The Fermi level is set at 0 eV and is indicated as a dashline. 71

5.13 The plots of the total density of states of the ternary phases of the metal nitrides. The Fermi level is set at 0 eV and is indicated as a dashline. 72

5.14 The plots of the total density of states of the ternary phases of the metal nitrides. The Fermi level is set at 0 eV and is indicated as a dashline. 73

5.15 The plots of the charge density distributions of the binary metal nitrides in the 001 plane. 74

5.16 The plots of the charge density distributions of the ternary metal nitrides in the 001 plane. 75

List of Tables

5.1 The calculated LDA and the GGA values of the equilibrium cell structures (Å)of the metal nitrides and their ternary phases at plane wave energy cutoff of 400eV. 47

5.2 Calculated LDA and the GGA values of the equilibrium cell structures (Å)of the metal nitrides with space group Pbnm and their ternary phases at plane wave energy cutoff of 500eV. 48

5.3 Calculated LDA and GGA values of the equilibrium structural properties and relative stability energies at plane wave energy cutoff of 400eV. 52

5.4 Calculated LDA and GGA values of the equilibrium structural properties and relative stability energies at plane wave energy cutoff of 500eV. 53

5.5 The LDA calculated values of the elastic constants and the Voigt isotropic moduli (the bulk modulus B, shear modulus G, Young modulus Y) in GPa, Poisson's ratio ν and the quotient of B/G. The experimental data for diamond are $G = 544$GPa, $B = 442$GPa, $Y = 1142$GPa and $\nu = 0.1$. Calculation were performed at a plane wave energy cutoff of 400eV. 55

5.6 The LDA calculated values of the elastic constants and the Voigt isotropic moduli (the bulk modulus B, shear modulus G, Young modulus Y) in GPa, Poisson's ratio ν and the quotient of B/G. The experimental data for diamond are $G = 544$GPa, $B = 442$GPa, $Y = 1142$GPa and $\nu = 0.1$. Calculation were performed at a plane wave energy cutoff of 500eV. 56

5.7 The GGA calculated values of the elastic constants and the Voigt isotropic moduli (the bulk modulus B, shear modulus G, Young modulus Y) in GPa, Poisson's ratio ν and the quotient of B/G. The experimental data for diamond are $G = 544$GPa, $B = 442$GPa, $Y = 1144$GPa and $\nu = 0.1$. Calculation were performed at a plane wave energy cutoff 400eV. 57

5.8 The GGA calculated values of the elastic constants and the Voigt isotropic moduli (the bulk modulus B, shear modulus G, Young modulus Y) in GPa, Poisson's ratio ν and the quotient of B/G. The experimental data for diamond are $G = 544$GPa, $B = 442$GPa, $Y = 1144$GPa and $\nu = 0.1$. Calculation were performed at a plane wave energy cutoff of 500eV. 58

1. Introduction

Quantum mechanical theories are reliable methods which can be used to predict new materials and explain their properties [1]. Quantum theory applications have progressed more slowly for solids than in molecules. Atomic theories have been spectroscopically validated, but in the case of solids there are many structural possibilities since solids are complex many-body ensembles of the order of 10^{23} strongly interacting particles. Aside from challenges experienced when using these methods, new physical descriptions and the availability of more high computing power have resulted in a successful theoretical description of existing hard materials as well as in the prediction of the new hard materials. To understand and describe accurately the physical properties of a material governed by the behaviour of a tiny almost massless electron, it is important to develop a valid quantum mechanical description. In this quantum mechanical model, it is necessary to solve the Schrödinger equation,

$$H\psi = E\psi(\mathbf{r_1}, ..., \mathbf{r_N}) \tag{1.1}$$

where H is the Hamiltonian acting on the N-particle wavefunction ψ. It is easy to extract information from the exact solution of the equation for a single electron atom but for a complex solid of the order of 10^{23} strongly interacting particles, is usually very difficult. Thus, it is unavoidable to introduce methods that approximate and reduce the size of the computational problem.

These modern theoretical quantum approaches are often referred to as the standard models for solids [1, 2]. Out of these standard models, one of the most popular forms involves pseudopotentials and assumes that the core electron of an atom remain unchanged when a solid structure is formed [2]. This has helped to reduce ambiguity in describing the properties of a model solid to one of using valence electrons interacting with a periodic array of positive ionic cores. These valence electrons get attracted to the positive cores through Coulombic attraction because these cores are made up of atomic core electrons that screen the nucleus. The potential that is obtained as a result of this, is called the pseudopotential [3].

Pseudopotentials are generated in various schemes starting from atomic wavefunction calculations. The Schrödinger equation is solved in density functional theory (DFT) to determine the pseudo-wavefunction. Different type of pseudopotential exit but the one utilized in this work is the projected augmented-wave (PAW) method implemented by Blöchl [4]. The PAW total energy functional is derived in a consistent way by applying the linear transformation (between soft nodeless pseudo (PS) wave function and the all-electron (AE) wave function) to the Kohn-Sham functional [5]. The PAW method has been proven to be effective in high performance computing for studying solids, surfaces and molecules. Further details will be provided in the course of this work.

Experimental synthesis and theoretical analyses carried out on the orthorhombic U_2S_3 tantalum nitride structure, Ta_2N_3 (space group **pbnm**, 62) by Zerr et al. [6] and Jiang et al. [7] predicted Ta_2N_3 to be potential superhard material. The properties of advanced metal nitrides M_2N_3 (where $M = Ta, V, Nb$) are explored in this work because of their novel future industrial application. Emphasis is also placed on the ternary phases of these advanced materials. Their relative stabilities are discussed as well as their densities of states. Despite the fact that these metal nitrides may often be seen as only the combination of the transition metals and nitrogen, some of them show interesting chemical and physical properties which are not notable in the metals and nitrogen alone. The binary nitrides of tantalum, Ta, have been known for their mechanical stability, chemical inertness and their possible application in microelectronics as a copper diffusion barrier [6].

Among these binary nitrides of tantalum is the high pressure TaN having $NaCl$ structure and the orthorhombic Ta_3N_5 [8]. Recently, the study of the ground state properties and phase stability of vanadium nitrides (VN, V_2N) [9] was carried out via a density functional electronic structure calculation. These compounds are important because of the potential applications of vanadium nitrides in hard coating, catalysis and optoelectronics [9]. The calculated phase stability of VN was revealed to be isoelectronic to niobium nitride, NbN, and these results are comparable with the ones observed by the recent phonon spectrum

study of the transition metal mononitrides by Isaev et al [10].

Following the fact that the structural, the relative stability and the elastic properties of material are being predicted, electronic structure studies have since become prominent in this field of research. It provides valuable information about the formation of alloys, their relative stability and various physical and chemical properties, quantitatively. The availability of high performance computing has given researchers an edge to elucidate the following unclear questions relating to; what atomic structure a material is composed of, its electronic properties and how the bond between atoms that constitute the material can be modified in order to create a novel hard material. Attempts are still in progress in applying first principles calculations employing density functional theory (DFT) to the problem of understanding the structural behaviour, phase diagram and mechanical properties of a material [11].

In this work, we employed the use of ab-initio quantum mechanical dynamic simulation using the projected augmented wave (PAW) method embedded in the Vienna Ab-initio Simulation Package (VASP) algorithm [12]. In the PAW method the pseudo-wave functions played the role of variational parameter and this is more simpler to treat than the all-electron function. The PAW method has proven its capability for studying surfaces, molecules and solids using high performance computing platforms. The projected augmented wave method is described in chapter 3. The ab-initio calculations used are based on the formalism of the density functional theory with the local density approximation (LDA) and the generalized gradient approximation (GGA). These functional were used in the treatment of the electron-electron interactions.

We present the format of this dissertation as follows: the subsequent chapter gives the overview of ultrahard materials and the concept of hardness. Chapter 3 covers reviews of the literature review of the theoretical background governing the computational models used. Chapter 4 describes the transition metal nitrides. In Chapter 5 we look at the techniques used in the computation of equilibrium properties and then present and discuss the computa-

tional results of the elastic, structural, electronic and relative properties of the orthorhombic metal nitrides of tantalum, vanadium and niobium. These results are compared with the experimental data available and finally, we conclude in Chapter 6.

2. Overview of Ultrahard Materials

The possibility of designing new low compressible materials with hardness similar or even larger than that of diamond has become a fundamental and technological challenge to chemists, physicists and many in material scientist community. This has intensified experimental and theoretical efforts in these fields [13, 14, 15, 16]. Ultrahard materials are of considerable practical importance as a result of their mechanical and thermal properties. They have a wide range of applications such as cutting tools, scratch resistant coating tools, in oil drilling, as gemstones, surgical knives, potential novel semiconductors, speaker components and one of the major industrial application of an ultrahard material is as superabrasives[13, 14, 15, 16].

There are three conditions that should be met before a material is certified ultrahard (or superhard) and these include: shorter bond length, higher bond density or electronic density and a greater degree of covalent bonding [16]. Ultrahard materials are distinguished into three classes, including the already synthesized and hypothetical phases [14]

- The ionic-covalent (such as oxides like corundum, Al_2O_3) and covalent compounds formed by the addition of the light elements from period 2 and 3 of the periodic table. The first group includes beryllium, boron, carbon, nitrogen, oxygen, aluminum, phosphorus and silicon.

- The second class are the specific covalent compounds which includes various crystalline and disordered carbon modifications. These carbon materials are regarded as special because of the existence of different types of chemical bond between the carbon atoms. For example, the cubic sp^3 carbon modification, diamond; and the trivalent sp^2 atoms of carbon, fullerites (C_{60}).

- The third class of ultrahard material includes the transition metals with light elements such as carbon C, boron B, oxygen O and nitrogen N - the partially covalent

compounds.

Although Beryllium Be falls in the same periodic row as B, C, N and O it has too few electrons to form strong bonding between atoms. A close look at the ultrahard materials that have already been synthesized and hypothetically predicted, and those having the possibility of becoming a potential candidate, reveals the fact that they consist of elements positioned in the middle group of the periodic table. These elements are known to have the smallest ionic, metallic or covalent radii and the largest cohesive forces between atoms. Typically, for the first group of the superhard materials, we have corundum (Al_2O_3) and the high pressure phase of SiO_2, stishovite. These are oxides that have the capability of forming a three dimensional rigid lattice with shortened covalent bonds [14]. The second group of the ultrahard materials are regarded as a special group and, because of the existence of different types of chemical bond between carbon atoms there is a great variety of carbon allotropes (diamond and graphite) and disordered phases [14]. Graphite crystallizes in a hexagonal crystal structure in trigonal coordinates as a result of the sp^2 hybridization of carbon atoms. Although the carbon bonds are shorter and stronger, only a weak van der Waals interactions hold them together allowing layers of graphite to cleave readily [17]

Diamond (strong covalent bond of tetrahedral sp^3 hybrid states) is still the hardest material to date. It occurs naturally as a gemstone and has been synthesized under extreme pressure-temperature conditions. It is number one on the Mohs scale, with scale value of 10 and has the lowest molar volume (3.4 cubic centimeters). Diamond is the most prized stone in jewelry because of it optical properties. It displays high thermal conductivity (2000W/mK) at room temperature, which is about four times as high as that of silver Ag and copper Cu. It is also known to be a good insulator under high temperature conditions and thus, is considered as an important candidate in electronics applications. All these unique properties of diamond make it indispensable in industry. It is used as a grinding tool, in cutting concrete, a polishing stone and in large scale for drilling rocks for oil wells. In addition, diamond has a low coefficient of friction and low thermal expansivity, high chemical and corrosive resistance

to acid and oxidizing substances. Diamond is considered to be transparent under visible and infrared light and can withstand ionization radiation [13, 17].

The strong chemical bond between each of the carbon atoms in a diamond structure results in its hardness by forming a regular cubic network linked to four other carbon atoms in its crystal lattice. Owing to the carbon's bond strength and its small atomic size, diamond has been able to form a denser mesh of atomic bonds than any other material. The best carbon source for diamond synthesis is graphite and as such, the characteristics of graphite are important [18]. The Vickers hardness for diamond varies from $70 - 140$GPa depending on the crystal type and the chosen crystal face [14]. High elastic constants and a very low Poisson's ratio have been recorded for diamond. From a theoretical approach, the study of hardness has been linked to high bulk modulus, B, and with recent research, it has also been correlated to the shear modulus, G, of the material. Among all the ultrahard materials ever synthesized or hypothetically predicted, diamond is still the leading system with high $B = 443$GPa and $G = 535$GPa values respectively [19]. Although diamond has been used traditionally to fulfill many industrial purposes, its application as a ferrous alloy cutting tool is limited. This is due to its chemical reaction with iron to produce iron carbide at high temperatures. This has prompted an increased efforts in the search for new bulk superhard materials that are not just harder than diamond but also more useful than diamond in certain circumstances [15].

Cubic boron nitride ($c - BN$) is the second hardest ultrahard material known. It has a structure that is similar in some respects to that of diamond and can be used to cut ferrous metals. However, cubic boron nitride does not occur in nature but has been synthesized under similar pressure range ($5.5 - 6.0$GPa) as that of diamond and at higher temperature (above 1950K). Cubic boron nitrides can withstand oxidation at extreme temperatures whereas diamond cannot. It has a low chemical reactivity, low density, high temperature, and high resistance to electricity and hardness that is only surpassed by that of diamond. Because of the improved resistance to oxidation, $c - BN$ allows high-speed cutting or grinding of steel-

based materials which cannot be done by diamond. It has a bulk modulus $B = 367$GPa and a shear modulus $G = 405$GPa [13, 16, 17]. However cubic boron nitride is not produced on a large scale basis due to difficult synthesis processes. This has called for more research to find new ultrahard materials.

With increasing pressure and temperature, most minerals are found to exhibit quite a number of structural phase transitions. From the well-known compound of SiO_2 (quartz at low temperature), a hard phase is the rutile-type SiO_2-stishovite, which was reported to be the third hardest material (33GPa) after diamond and $c-BN$, but it has not yet been stabilized for technological use [13]. The high bulk moduli and hardness of stishovite are due to silicon atoms in this compound that are octahedrally (sixfold) coordinated, which is different from the fourfold coordination of the low pressure phase of SiO_2, (quartz). The oxide B_6O possesses a high hardness (Vickers hardness of $32-38$GPa) [14]. B_6O is as hard as the cubic boron nitride and has a fracture toughness similar to that of diamond. It can be synthesized at much lower pressure (even at ambient pressure) as compared to that for diamond and $c-BN$. It combines hardness with low density, high thermal conductivity and high chemical inertness [20]. The wurtzite and the hexagonal boron nitrides ($w-BN$ and $h-BN$, respectively) are well known as having high hardness and high elastic moduli.

Other covalent materials such as the compounds of boron with carbon, silicon and phosphorus (examples B_4C, BP and B_4Si) as well as silicon nitride (Si_3N_4) are of great interest. In particular Si_3N_4, is an important new synthetic hard material among new ceramics. It has outstanding high oxidation and temperature resistant properties and therefore many industrial applications [21]. The recently synthesized cubic spinel structure phase of Si_3N_4 with high calculated shear and bulk elastic moduli [22] has proven that the preparation of new dense and hard materials can be achieved under high pressure. The hardness value of the cubic phase $\gamma-Si_3N_4$ is closer to that of the SiO_2-stishovite but significantly below that of the diamond and cubic boron nitride.

Another material that has been suggested as an ultrahard material with bulk modulus

(427GPa) comparable to that of diamond is C_3N_4. However, with the exciting research activities to search for and synthesize C_3N_4, no conclusive evidence have been provided yet [21]. The hexagonal $\beta - C_3N_4$ phase has been computed theoretically using semi-empirical methods and the bulk modulus value estimated as 483GPa, which is higher than that diamond [19]. The hexagonal $\beta - C_3N_4$ was considered to have the same structure as the hexagonal $\beta - Si_3N_4$ and this led to the speculation that C_3N_4 may also exist in the spinel nitride phase [21]. Transition metal compounds show very high bulk modulus and cohesive energy, which is directly linked to their valence electron between the bonding and antibonding region within the partially filled electron states. This makes them a potential candidate for ultrahard materials. It is still fascinating that with all the materials (either synthesized or reported), having bulk modulus close to or even greater than that of diamond, diamond remains the hardest material ever known. This brings us to the conclusion that the search for new materials will still be ongoing even in centuries to come.

2.1 Concept of Hardness

In designing a new ultrahard material, it is useful to consider the type of structural changes a material can undergo when subjected to a load. These changes can be in the form of reversible or irreversible deformation which are classified as elastic or plastic deformations [15]. An ultrahard material is usually defined as a material with hardness value of above 40GPa and among all known phase compounds only diamond (90GPa) and $c-BN$ (50GPa) exceeds this value. Hardness is a complex concept and from a mechanical point of view, it is seen as one of the quantitative parameters that describe the resistance of a material towards elastic (reversible) or plastic (irreversible) deformations. Deformation occurs when the shear stress exceeds the yield stress of the said material. Hardness is influenced strongly by various parameters: porosity, pressure, temperature, dislocations, impurities, microstructural texture and grain size. It was first defined experimentally, as the ability of one material

to scratch another with the use of certain substance from talc = 1 to diamond = 10, this correspond to the Mohs scale. Regrettably, a single step on the Mohs scale became highly nonlinear in terms of hardness measurement. In addition, from the experimental viewpoint, the Moh scale is less reliable since materials with comparable but not equal hardness are able to scratch each other.

The methods for measuring the hardness value of a material involve subjecting the material to an indentation by a hard indenter, usually diamond loaded perpendicular to a planar surface of the material being tested. The hardness value depends on the geometry of the indenter and the parameter associated with the test, as well as the environmental condition. There are various methods that utilize this concept: these include the Rockwell, the Brinell, the Knoop and Vickers indenter [13, 14, 17, 23, 24]. Hardness determined from these procedures depends on the ratio of the load in the framework of the method, to the indentation area. The hardness value of metal forging and castings having large grain structures are usually determined by the Brinell hardness testing. A Rockwell testing measures the penetration produced by a major load. This test was originally designed for use on thin metallic components and coatings but in addition to that, it can also test for data on bulk ceramics [25].

A Vickers hardness test uses the diamond square-based pyramid indenter in determining the hardness of a material. The Vickers hardness is defined as the ratio of the applied load P to the surface area of the impression whereas the Knoop hardness is the ratio of the load P to the projectal area of the impression. These are expressed mathematically as

$$H_V = \frac{1.8544P}{d^2}, \tag{2.1}$$

$$H_K = \frac{14.229P}{l^2}. \tag{2.2}$$

l is the long diagonal of the rhombus-based diamond pyramid of the Knoop indenter and d, the diagonal of the square-based diamond pyramid for the Vickers indenter. In order to compare hardness values from different testing methods, it is important to reference the exact test method and conditions [17]. Hard materials are of tremendous importance to industrial

application and thus, are still undergoing intensive investigation; both experimentally and in theoretical calculations. The combination of hardness with other vital properties such as chemical inertness and low-cost of synthesis is of great interest too.

The concept of hardness is visualized in terms of two different contributions: intrinsic and extrinsic contributions. The latter includes the grain boundary, residual stress and solution precipitation whereas, the former are based on the nature of the bonding structure of the material (that is, the strength of the chemical bond between atoms) which is reflected by the high elastic moduli. These bonds are mostly covalent in nature and at times it is possible for the bonds to be ionic-covalent or metallic bond. The ionic-covalent bonds are less deformable than those of the metal. The covalent materials are much better candidates for high hardness because of the localized electronic interaction between the atoms. In addition, the dislocation mobility in the material needs to be as small as possible [26].

Although, the definition of hardness and the process of its measurement seem ambiguous, it has been, and is still described theoretically in terms of elastic bulk and shear moduli. This is not uncommon as hardness is related to physical properties like cohesive energy, ionicity, melting point, band gaps and thus, can be studied indirectly [24]. There have been a series of theoretical computations aimed at finding materials with high values of bulk modulus B and shear modulus G in the last two decades [16]. In fact, the aim of designing hardness is to use the knowledge of plastic resistance and elastic stiffness to propose new ultrahard materials [15]. Bulk modulus B is the most simple measure of elastic stiffness. It measures the resistance to volume change and this resistance to elastic strain depends on the valence electron density, VED (electrons/unit volume). This implies that high bulk modulus equals high VED [26]. A recent investigation carried out, revealed a correlation between VED and hardness and this led to a speculation that hardness can be understood in terms of the electronic band structure of a material [16]. Bulk modulus B is the reciprocal value of compressibility K, how a material responds to hydrostatic pressure [24]. For an ultrahard material, compressibility K is a very important property because it gives information on

the strength of the material, the electronic structure and the chemical bonding [18]. From Hooke's law, the bulk modulus, B is related to the applied stress σ and elastic strain ε by

$$B = \frac{d\sigma}{d\varepsilon}, \tag{2.3}$$

where σ is the derivative of the binding energy E_b and the bond length l given as

$$\sigma = \frac{dE_b}{dl}. \tag{2.4}$$

By implication, there is a clear relation between the bulk modulus, the binding energy and the interatomic bond length given as

$$B = \frac{d^2E_b}{dl^2}. \tag{2.5}$$

Thus, a material with short interatomic forces leads to a high bulk modulus as well as high bond energy and valence electron density. This was proposed by Marvin Cohen in early 1990s [17, 19]. In the last two decades, bulk moduli have been used as a rough scale to measure the hardness of a material because it was cheaper to compute in terms of the efficient use of computer time. On this scale, materials with the value of bulk modulus exceeding 250GPa were considered as being ultrahard materials [13]. However the correlation that existed between the bulk modulus and hardness, were still limited. For instance, the bulk modulus of hypothetical hexagonal phase of $\beta - C_3N_4$ is higher than that diamond but does not necessarily mean it is in any way near the hardness of diamond[14].

However, there is this general intuition that hardness of a material depends strongly on the creation and movement of dislocations in response to the shear stress produced by an indentation. As the shear strain needed for the dislocation motion is related directly to the elastic shear modulus of the deformed material. The elastic shear modulus measures the material's resistance to shape change. It is not accidental, that there is a strong correlation between the elastic shear modulus and hardness because, the mechanical tests are linked with deformations that consist of shear component, and the fact that atomic forces are correlated to elastic and plastic deformation [13, 14, 15, 16]. The compilation of experimental data for

different materials shows that elastic shear modulus is a better predictor of hardness than the elastic bulk modulus [24].

3. Theoretical Background

In describing and predicting properties of materials, atomistic simulations, electronic structure theory (quantum mechanical method) has become increasingly vital over the years, especially with the present-day high performance computers. Among these properties are the total energy, the valence electron density, the force between atoms and so on. The origin of the theory of electronic structure of solids is the nonrelativistic Schrödinger equation for many-body wave function ψ, expressed as

$$\left[\frac{-\hbar^2}{2m}\sum_j \nabla_j^2 - \sum_{j,l}\frac{Z_l e^2}{|r_j - R_l|} + \frac{e^2}{2}\sum_{j\neq j'}\frac{1}{|r_j - r_j'|}\right]\psi = E\psi, \tag{3.1}$$

where $\mathbf{r_j}$ are the electron positions and $\mathbf{R_l}, \mathbf{Z_l}$ the positions and atomic numbers of the nuclei; $\mathbf{E}$ is the energy and $\mathbf{e}, \hbar$, and $\mathbf{m}$ are fundamental constants [27]. The Hamiltonian for the entire system is made up of the kinetic energy of the electrons in the system, electrons and nuclei including their interaction energy. The theory of electronic structure is divided into two classes: the ab-initio methods and the semi-empirical methods. However, there is an economy of scale to ab-initio total energy calculation because many physical properties are related to the total energies and this makes this method very important in computational material science and solid state physics. The cornerstone of this development was laid by density functional theory (DFT).

The objective of this chapter is to explicate the mathematical and physical background behind the computation of the properties of the advanced metal nitrides M_2N_3. We discuss the density functional theory, which is an alternative approach to the theory of electronic structure. The Hohenberg-Kohn (HK) and the Kohn-Sham (KS) approach are discussed as well as the treatment of the exchange-correlation energy with local density approximations (LDA) and the generalized gradient approximations (GGA). We also discuss the pseudopotential wave methods.

3.1 Density Functional Theory (DFT)

Density functional theory is a relatively recent theory that scientists have developed to replace the crude theory of electronic structure in terms of the electron density distribution $\mathbf{n}(\mathbf{r})$, the Thomas-Fermi theory [28]. However useful the Thomas-Fermi theory is, in describing some qualitative trends for total energies of atoms, it fails to answer questions relating to the essential physics and chemistry, such as shell structures of atoms, binding of molecules and thus, fall short of the goal of a useful description of electrons in matter [29].

The fundamental principle of density functional theory (DFT) is that any properties of the many-body system can be expressed not in terms of a wavefunction but as a functional of the ground state electron density itself, which is a simpler object to deal with than the wavefunction. The electron density $\mathbf{n}(\mathbf{r})$ is a function of three coordinates $(\mathbf{r}, \theta, \psi)$ and it determines the electronic structure of the system of interacting electrons in an external potential $\mathbf{V_{ext}}(\mathbf{r})$ generated by the core atoms. It is expressed as,

$$\mathbf{n}(\mathbf{r}) \quad = \quad \int \psi^*(\mathbf{r_1}, \mathbf{r_2}, ..., \mathbf{r_N})\psi(\mathbf{r_1}, \mathbf{r_2}, ...\mathbf{r_N})\mathbf{dr_1}, \mathbf{dr_2}, ...\mathbf{dr_N}. \tag{3.2}$$

Density functional theory has some strengths and weaknesses. It has high computational efficiency and good accuracy, hence it is fast. This is so because DFT with basis sets $\psi_\mathbf{i}$ and the number of electron in a solid scales like the Hartree-Fock of self consistent field theory [30]. In density functional theory, we have a set of working equations called the Kohn-Sham total energy functional for a set of occupied electronic states ψ_i which we shall discuss later.

$$\left[\frac{-\hbar^\mathbf{2}}{\mathbf{2m}}\nabla^\mathbf{2} - \sum_\mathbf{i}\frac{\mathbf{Z_i e^2}}{|\mathbf{r}-\mathbf{R_l}|} + \mathbf{e^2}\int \mathbf{n}(\mathbf{r'})\frac{\mathbf{1}}{|\mathbf{r}-\mathbf{r'}|}\mathbf{dr'} + \mathbf{U_{xc}}(\mathbf{n}(\mathbf{r}))\right]\psi_\mathbf{i} \quad = \quad \varepsilon_\mathbf{i}\psi_\mathbf{i}. \tag{3.3}$$

The Kohn-Sham total energy is decomposed into four contributions: a kinetic energy, a nuclear attraction potential, a Coulombic attraction of the electrons in the electronic state $\psi_\mathbf{i}$ with the other electrons in that system and finally, the exchange-correlation potential $\mathbf{U_{xc}}(\mathbf{n}(\mathbf{r}))$ that covers all the many-body interactions. The exchange-correlation energy is

considered the heart of DFT. In contrast to what we see in Hartree-Fock (HF) theory

$$\left[\frac{-\hbar^2}{2m}\nabla^2 - \sum_i \frac{Z_i e^2}{|r - R_l|} + \sum_{j=occ}(J_j - K_j)\right]\psi_i = \varepsilon_i \psi_i. \tag{3.4}$$

The third term on the left hand side represents the coulomb exchange integral expressed in terms of the occupied states ψ_i [30]. HF theory only describes the interaction of the individual electrons with the nuclei and all other electrons in the system while DFT starts with the consideration of the entire electronic system. DFT has successes which are notable to the local density approximation (LDA) and the generalized gradient approximation (GGA) with the Kohn-Sham method [29]. This has left a tremendous interest in DFT as the most promising method for accurate, practical method of studying the theory of material. Density functional theory was first proposed by Hohenberg and Kohn [31] and later improved by Kohn and Sham [32].

3.2 Hohenberg-Kohn Theorems

The crux of this work is the proof that an exact formal variational principle for the ground state energy is developed, in which the charge density $n(r)$ is the variable function of the system. The Hohenberg-Kohn theorem states that for a given nondegenerate ground state wavefunction ψ_i, all the physical properties of a system of interacting electrons are determined by its unique ground state charge density distribution $n(r)$ [31]. This property holds irrespective of the precise form of the electron-electron interaction.

The proposal is that the ground state electron density describing any N-electron system is in unique correspondence with the external potential $V(r)$, including any problem of the electrons and the fixed nuclei, where the Hamiltonian H can be written as

$$H = -\frac{\hbar^2}{2m}\sum_i \nabla_i^2 + \sum V(r_i) + \frac{e^2}{2}\sum_{i \neq j}\frac{1}{|r_i - r_j|}. \tag{3.5}$$

Since $\mathbf{H}$ determines the energy $\mathbf{E}$ and the wavefunction of the system, it implies that the ground state density therefore determines all the properties of the system. The fact that $\mathbf{n(r)}$ specifies where the nuclei are located in that system and the steepness of the potential specify the nuclear charges that gives $\mathbf{n(r)}$. To prove this theorem:

Let suppose we know $\mathbf{n(r)}$ at all points $\mathbf{r}$, then $\mathbf{n(r)}$ determines the number of electrons $\mathbf{N}$ in that system since $\mathbf{N} = \int \mathbf{n(r)d^3r}$. By implication, if we know $\mathbf{N}$, then we can write the kinetic and the electron-electron repulsion parts of the Hamiltonian as in equation (3.5). Let also assume that there are two distinct potentials $\mathbf{V_1(r)}$ and $\mathbf{V_2(r)}$ which forms two Hamiltonian $\mathbf{H_1}$ and $\mathbf{H_2}$ and when potentials are used in these Hamiltonians to solve the Schrödinger equation for their ground state, produces $\mathbf{E_1}, \psi_\mathbf{1}(\mathbf{r})$ and $\mathbf{E_2}, \psi_\mathbf{2}(\mathbf{r})$. Finally, assume that $\psi_\mathbf{1}$ and $\psi_\mathbf{2}$ have the same one-electron density

$$\int |\psi_\mathbf{1}|^\mathbf{2} \mathbf{dr_2, dr_3, ...dr_N} = \mathbf{n(r)} = \int |\psi_\mathbf{2}|^\mathbf{2} \mathbf{dr_2, dr_3, ...dr_N}. \tag{3.6}$$

Taking $\psi_\mathbf{1}$ as a trial variational wavefunction for the Hamiltonian $\mathbf{H_2}$, we find that

$$\mathbf{E_2} = \langle \psi_\mathbf{2} | \mathbf{H_2} | \psi_\mathbf{2} \rangle < \langle \psi_\mathbf{1} | \mathbf{H_2} | \psi_\mathbf{1} \rangle = (\psi_\mathbf{1}, (\mathbf{H_1} + \mathbf{V_2} - \mathbf{V_1}) \psi_\mathbf{1}) \tag{3.7}$$

so that,

$$\mathbf{E_2} < \mathbf{E_1} + \int [\mathbf{V_2} - \mathbf{V_1}] \mathbf{n(r) d^3 r}. \tag{3.8}$$

Also, taking $\psi_\mathbf{2}$ as a trial variational wavefunction for $\mathbf{H_1}$, we obtain

$$\mathbf{E_1} = \langle \psi_\mathbf{1} | \mathbf{H_1} | \psi_\mathbf{1} \rangle < \langle \psi_\mathbf{2} | \mathbf{H_1} | \psi_\mathbf{2} \rangle = (\psi_\mathbf{2}, (\mathbf{H_2} + \mathbf{V_1} - \mathbf{V_2}) \psi_\mathbf{2}) \tag{3.9}$$

so that,

$$\mathbf{E_1} < \mathbf{E_2} + \int [\mathbf{V_1} - \mathbf{V_2}] \mathbf{n(r) d^3 r} \tag{3.10}$$

summing up equations (5.1) and (5.2), we obtain

$$\mathbf{E_1} + \mathbf{E_2} < \mathbf{E_2} + \mathbf{E_1} \tag{3.11}$$

This is clearly a contradiction unless the energies are degenerate and thus, no two wavefunctions having different Hamiltonians can give the same electron density $\mathbf{n}(\mathbf{r})$. This also suggest that, there cannot be two different external potentials that give the same electron density, $\mathbf{n}(\mathbf{r})$ for their ground state [32]. The proof also indicates that the total information about the stationary system; eigenvalues, Hamiltonian and wavefunctions are contained within the electron density since it completely specifies the external potential.

It is evident from the proof that $\mathbf{n}(\mathbf{r})$ determines $\mathbf{N}$ and $\mathbf{V_{ext}}(\mathbf{r})$ and hence all properties of the ground state. The big question is, how is the kinetic energy $\mathbf{T}[\mathbf{n}(\mathbf{r})]$ and the electron-electron interaction energy expressed in terms of $\mathbf{n}(\mathbf{r})$?. It is easy to see that

$$\mathbf{V_{ext}}[\mathbf{n}(\mathbf{r})] = \int \mathbf{V_{ext}}(\mathbf{r})\mathbf{n}(\mathbf{r})\mathbf{dr}. \tag{3.12}$$

The second Hohenberg-Kohn theorem provides the energy variational principle. The energy functional in terms of the density $\mathbf{n}(\mathbf{r})$ can be defined as

$$\mathbf{E}[\mathbf{n}(\mathbf{r})] = \int \mathbf{V_{ext}}(\mathbf{r})\mathbf{n}(\mathbf{r})\mathbf{dr} + \mathbf{F}[\mathbf{n}(\mathbf{r})], \tag{3.13}$$

where $\mathbf{F}[\mathbf{n}(\mathbf{r})]$ is the universal functional of the density $\mathbf{n}(\mathbf{r})$. It includes all the internal energies, kinetic energy of the interacting electron system and is valid for any number of electrons and any external potential. Applying the variational principle when the electron density corresponds exactly to that induced by the external potential, the total energy functional $\mathbf{E}[\mathbf{n}(\mathbf{r})]$ becomes the ground state energy (at minimum energy) and the density $\mathbf{n}(\mathbf{r})$ that minimizes the functional energy is the exact ground state density [29]. The universal functional $\mathbf{F}[\mathbf{n}(\mathbf{r})]$ can then be broken down into

$$\mathbf{F}[\mathbf{n}(\mathbf{r})] = \frac{\mathbf{1}}{\mathbf{2}} \int \frac{\mathbf{n}(\mathbf{r_1})\mathbf{n}(\mathbf{r_2})}{|\mathbf{r_1} - \mathbf{r_2}|}\mathbf{dr_1 dr_2} + \mathbf{T}[\mathbf{n}(\mathbf{r})] + \mathbf{U_{xc}}[\mathbf{n}(\mathbf{r})] \tag{3.14}$$

where the first term is the Hartree energy followed by the kinetic energy and then $\mathbf{U_{xc}}$ is the exchange-correlation energy. These two parameters are more difficult to express in terms of the electron density. $\mathbf{T}[\mathbf{n}(\mathbf{r})]$ is determined by the Kohn-Sham theory whereas the $\mathbf{U_{xc}}$ uses the local density approximation. However, Hohenberg-Kohn theorem has proved the

possibility of computing the properties of a system using the ground state density but fail to proffer solution on how to compute the ground state density. This deficiency is remedied by the Kohn-Sham self-consistent equations.

3.3 Kohn-Sham Approach to Density Functional Theorem

Today, density functional theory has become the most widely used theory for electronic structure calculations because of the approach proposed by Kohn-Sham [32]. The main concern of the Kohn-Sham approach is to provide a framework for finding the exact density $\mathbf{n}(\mathbf{r})$ and energy of the ground state of a many-body electron problem, by solving a set of self-consistent single particle Schrödinger equations. To achieve this, Kohn-Sham utilized the variational functional that includes the total energy functional at minimum energy in the Hohenberg-Kohn (HK) approach. Since there was no unambiguous guidance as to the exactness of $\mathbf{E}[\mathbf{n}(\mathbf{r})]$ from the HK formalism, Kohn-Sham made some assumptions in order to calculate the properties of a physical system. The KS method assumes that the ground state density of non-interacting electron moving in an effective potential due to all the other electrons, is the same as the density of the original system where the electrons do interact [11]. Since the electron density determines the position and atomic number of the nuclei, these quantities are identical in both systems (the interacting and non-interacting system). From the HK formalism, it has been shown that the total ground state energy of an interacting inhomogeneous electron can be written as

$$\mathbf{E}[\mathbf{n}(\mathbf{r})] = \mathbf{T}[\mathbf{n}(\mathbf{r})] + \int \mathbf{V_{ext}}(\mathbf{r})\mathbf{n}(\mathbf{r})\mathbf{dr} + \frac{\mathbf{1}}{\mathbf{2}} \int \frac{\mathbf{n}(\mathbf{r})\mathbf{n}(\mathbf{r}')}{|\mathbf{r}-\mathbf{r}'|}\mathbf{drdr}' + \mathbf{U_{xc}}[\mathbf{n}(\mathbf{r})], \quad (3.15)$$

where $\mathbf{T}[\mathbf{n}(\mathbf{r})]$ is the kinetic energy of the non-interacting electron gas with the density $\mathbf{n}(\mathbf{r})$. This is followed by the external potential energy due to the nuclei (the Hartree energy) and lastly, the exchange-correlation energy $\mathbf{U_{xc}}$ which contains all the many-body effects. It is

instructive to mention that $\mathbf{U_{xc}}$ contains the effects of the electron-electron interaction and the positive correlation contribution to the kinetic energy (an effect of the uncertainty and Pauli principles). It also contains part of the ion-electron interaction which is not considered by the external and Hartree potentials.

Assuming the solution of the Kohn-Sham equations for the ground state is viewed as a problem of minimization with respect to the density $\mathbf{n(r)}$; varying equation (3.15) with $\mathbf{n(r)}$, we obtain

$$\mu = \frac{\delta \mathbf{T[n]}}{\delta \mathbf{n(r)}} + \frac{\delta \mathbf{U_{xc}[n]}}{\delta \mathbf{n(r)}} + \frac{\mathbf{1}}{\mathbf{2}} \int \frac{\mathbf{n(r')}}{|\mathbf{r} - \mathbf{r'}|} \mathbf{dr'} + \mathbf{V_{ext}(r)}. \tag{3.16}$$

Where, $\mu = \dfrac{\delta \mathbf{E[n]}}{\delta \mathbf{n(r)}}$ is the chemical potential connected with the limitation of the density to yield the correct number of electrons $\mathbf{N}$. From equation (3.16), we define the effective potential term as:

$$\mathbf{V_{eff}(r)} = \mathbf{V_{ext}(r)} + \mathbf{V_H(r)} + \mathbf{V_{xc}}. \tag{3.17}$$

Where,

$$\mathbf{V_{xc}(r)} = \frac{\delta \mathbf{U_{xc}}}{\delta \mathbf{n(r)}}, \tag{3.18}$$

$$\mathbf{V_H(r)} = \frac{\mathbf{1}}{\mathbf{2}} \int \frac{\mathbf{n(r')}}{|\mathbf{r} - \mathbf{r'}|} \mathbf{dr'}. \tag{3.19}$$

The effective potential energy contains the external potential energy $\mathbf{V_{ext}}$ due to the nuclear interaction, the Hartree potential $\mathbf{V_H}$ and the exchange-correlation potential $\mathbf{V_{XC}}$. But we know that, the minimization of the total ground state energy with respect to $\mathbf{n(r)}$ leads to the effective single particle Schrödinger equation

$$\left[-\frac{\hbar^{\mathbf{2}}}{\mathbf{2m}} \nabla^{\mathbf{2}} + \mathbf{V_{eff}(r)} \right] \psi_{\mathbf{i}} = \varepsilon_{\mathbf{i}} \psi_{\mathbf{i}}, \tag{3.20}$$

and this is solved self-consistently on the condition that

$$\mathbf{n(r)} = \sum_{\mathbf{i=1}} |\psi_{\mathbf{i}}|^{\mathbf{2}}, \tag{3.21}$$

where the wavefunction $\psi_{\mathbf{i}}$ is normalized so that the sum goes over the lowest $\mathbf{N}$ normalized solutions of equation (3.20) for $\mathbf{N}$ number of particles [33]. We can then write equation (3.15) as

$$\sum_{\mathbf{i=1}}^{\mathbf{N}} \varepsilon_{\mathbf{i}} \;=\; \mathbf{T}[\mathbf{n}(\mathbf{r})] + \int \mathbf{V_{eff}}(\mathbf{r})\mathbf{n}(\mathbf{r})\mathbf{dr}. \tag{3.22}$$

Substituting equations (3.17) and (3.22) into (3.15), the total ground state energy is given by

$$\mathbf{E}[\mathbf{n}] \;=\; \sum_{\mathbf{i=1}}^{\mathbf{N}} \varepsilon_{\mathbf{i}} - \frac{\mathbf{1}}{\mathbf{2}} \int \frac{\mathbf{n}(\mathbf{r})\mathbf{n}(\mathbf{r'})}{|\mathbf{r}-\mathbf{r'}|}\mathbf{drdr'} - \int \mathbf{V_{xc}}\mathbf{n}(\mathbf{r})\mathbf{dr} + \mathbf{U_{xc}}[\mathbf{n}(\mathbf{r})]. \tag{3.23}$$

In practical application, the Kohn-Sham method leads to the self-consistent solution of the $\mathbf{N}$ lowest eigenvalues $\varepsilon_{\mathbf{i}}$ and the corresponding single particle wavefunctions $\psi_{\mathbf{i}}(\mathbf{r})$ of the coupled set of Kohn-Sham equations given by equations (3.17) - (3.21). In principle, the Kohn-Sham eigenvalues are not really the energies of the single particle electron states but rather the artifact of mapping of the interacting system onto the KS system [11]. The exact ground state density is obtained by iterating the self-consistent equations. Assuming that $\mathbf{V_{xc}}$ is the exact exchange-correlation potential, taking the derivative of the functional with respect to the density gives a result that includes the exact effect of exchange-correlation [27]. The practical problem of solving the many-body problem involves the choice of a good approximation of the exchange-correlation energy. The approximations that are of interest in this work are the local density approximation (LDA) and the generalized gradient approximation (GGA).

3.4 Local Density Approximation (LDA)

The exchange-correlation potential $\mathbf{V_{xc}}$ proposed by Kohn and Sham [32] is vital for the success of density functional theory approach. It is a functional derivative of the exchange-

correction energy with respect to the local density, $\mathbf{n(r)}$ at a region $\mathbf{r}$. It is expressed as

$$\mathbf{V_{xc}} = \frac{\delta \mathbf{U_{xc}}[\mathbf{n(r)}]}{\delta \mathbf{n(r)}} \tag{3.24}$$

In a homogeneous system, the exchange-correlation potential depends on the value of the electron density whereas in the nonhomogeneous system, the value of the exchange correlation potential at the points $\mathbf{r}$ depends not only on the value of density at $\mathbf{r}$, but also on its variation close to $\mathbf{r}$ and therefore, we write the exchange-correlation potential as

$$\mathbf{V_{xc}}[\mathbf{n(r)}] = \mathbf{V_{xc}}\left[\mathbf{n(r)}, \nabla \mathbf{n(r)}, \nabla(\nabla \mathbf{n(r)}), ...\right] \tag{3.25}$$

The inclusion of the gradient of the density makes the solution of DFT to be difficult. Assuming that the exchange-correlation energy leads to an exchange-correlation potential on the value of the density $\mathbf{n(r)}$ in $\mathbf{r}$ and not on its gradient, then the simplest method by which we can obtain this contribution is through the use of the local density approximation (LDA) [32]. The local density approximation (LDA) states that, for a given region ($\mathbf{r}$) of a material where the charge density is slowly varying, the exchange correlation energy at that point can be considered the same as that for a locally homogeneous electron gas that has the same charge density, $\mathbf{n(r)}$ at that region [11]. In this case, we can now write $\mathbf{U_{xc}^{LDA}}[\mathbf{n(r)}]$ as

$$\mathbf{U_{xc}^{LDA}}[\mathbf{n(r)}] = \int \mathbf{u_{xc}(r)n(r)d^3r}$$

with

$$\mathbf{u_{xc}(r)} = \mathbf{u_{xc}^{hom}}[\mathbf{n(r)}]$$

where $\mathbf{U_{xc}^{LDA}}[\mathbf{n(r)}]$ is the exchange-correlation functional and $\mathbf{u_{xc}(r)}$ is the exchange correlation energy per electron at the region, $\mathbf{r}$ in the electron gas with density $\mathbf{n(r)}$. The exchange-correlation potential for the functional (LDA) will the correspond to

$$\mathbf{V_{xc}^{LDA}} = \frac{\delta \mathbf{U_{xc}^{LDA}}[\mathbf{n(r)}]}{\delta \mathbf{n(r)}}$$

The exchange effect are usually added in terms based on the homogeneous electron gas calculation and this gives rise to a new form of the exchange-correlation energy

$$\mathbf{u_{xc}}[\mathbf{n(r)}] = -\frac{\mathbf{3}}{\mathbf{4}}\left(\frac{\mathbf{3}}{\pi}\mathbf{n(r)}\right)^{\frac{\mathbf{1}}{\mathbf{3}}}$$

For a spin-polarized DFT, the LDA becomes the local spin density approximation (LSDA) with the expression

$$\mathbf{U_{xc}^{LSD}}[\mathbf{n_\uparrow}, \mathbf{n_\downarrow}] = \int \mathbf{d^3r}\ \mathbf{n}(\mathbf{n_\uparrow}, \mathbf{n_\downarrow})\mathbf{u_{xc}^{hom}}[\mathbf{n_\uparrow}, \mathbf{n_\downarrow}]$$

where $\mathbf{n_\uparrow}$ and $\mathbf{n_\downarrow}$ are the densities for spin up and spin down. In principle, the local density approximation tend to ignore correction to the exchange-correlation energy at a region due to inhomogeneities in the electron density [29]. The local density approximation assumes that the exchange-correlation energy is purely local. There have been several parameterizations of $\mathbf{u_{xc}}$ reported in literature, some of which includes Kohn-Sham [32] and Perdew et al. [34]. For this work, the LDA functional uses the parameterizations of the exchange-correlation functional by Perdew and Zunger [35] based on Quantum Monte-Carlo simulation for the homogeneous electron gas by Ceperley and Alder [36]. Apparently, LDA works well even in a system where the charge density is rapidly varying by adding an empirical energy - a strong inter-electron correlation [18].

Although LDA is relatively simple, it is surprisingly accurate and forms the core of most modern density functional theory approaches. However, LDA tends to under predict atomic ground state energies while over estimating the binding energies (the cohesive energies). For this reason, an improvement has been made upon LDA by including the dependence of the charge density gradient. This is an approximation called the generalized gradient approximation which will be discussed below.

3.5 Generalized Gradient Approximation (GGA)

According to Perdew et al. [37], the density functional theory by Kohn-Sham is widely used for self-consistent field electronic structure calculations of the ground state properties of solids. The approximations which account for the spatial variation of density are called the generalized gradient approximations (GGA's). The GGA's for the exchange-correlation energy improves upon the local spin density (LSD) approximations. It is expressed as

$$\mathbf{U_{xc}^{GGA}}[\mathbf{n}_\uparrow(\mathbf{r}), \mathbf{n}_\downarrow(\mathbf{r})] = \int \mathbf{d^3r}\ \mathbf{f}\left(\mathbf{n}_\uparrow(\mathbf{r}), \mathbf{n}_\downarrow(\mathbf{r}), \nabla\mathbf{n}_\uparrow(\mathbf{r}), \nabla\mathbf{n}_\downarrow(\mathbf{r})\right),$$

where $\mathbf{n}_\uparrow$ and $\mathbf{n}_\downarrow$ are the densities of spin up and spin down respectively. In the paper presented by Perdew, Burke and Ernzerhof [37], only the exchange-correlation energy $\mathbf{U_{xc}} = \mathbf{U_x} + \mathbf{U_c}$ which is expressed as a functional of the electron spin densities $\mathbf{n}_\uparrow$ and $\mathbf{n}_\downarrow$ are approximated. GGAs do not provide a steady improvement over the local density approximation in all types of system but in analogy to the local spin density approximation, it tends to improve upon the total energy, atomization energies, energy barriers and the structural energy differences. Generalized gradient approximations also expand the bond length, an effect which sometimes corrects the local spin density approximation [37].

In this work, we utilized the PBE-generalized gradient approximation as parameterized by Perdew *et al.*[37] to do calculations of ground state properties of the advanced metal nitrides M_2N_3. To facilitate practical calculation in GGA, the homogeneous exchange-correlation energy, $\mathbf{u_{xc}^{hom}}$ and $\mathbf{f}$ must be parameterized analytic functions. The GGA for correlation is first written in the form

$$\mathbf{U_c^{GGA}}[\mathbf{n}_\uparrow(\mathbf{r}), \mathbf{n}_\downarrow(\mathbf{r})] = \int \mathbf{d^3r}\ \mathbf{n}(\mathbf{r})\left[\mathbf{u_c^{hom}}(\mathbf{r_s}, \zeta) + \mathbf{H}(\mathbf{r_s}, \zeta, \mathbf{t})\right]$$

with

$$\mathbf{H} = \left(\frac{\mathbf{e^2}}{\mathbf{a_0}}\right)\gamma\phi^{\mathbf{3}}\ln\left(\mathbf{1} + \frac{\beta}{\gamma}\mathbf{t^2}\left[\frac{\mathbf{1} + \mathbf{At^2}}{\mathbf{1} + \mathbf{At^2} + \mathbf{A^2t^4}}\right]\right)$$

where $\mathbf{r_s}$ is the local Seitz radius, ζ is the relative spin polarization and $\mathbf{t} = \frac{|\nabla\mathbf{n}|}{/\mathbf{2}\phi\mathbf{k_s n}}$ is a dimensionless density gradient, ϕ is the spin-scaling factor, $\mathbf{k_s}$ is the Thomas-Fermi screening

wave number and the quantity β is the same as for the exchange term $\beta = \mathbf{0.066725}$ and $\gamma = \mathbf{0.031091}$. To show non-locality of the GGA, we define the enhancement factor $\mathbf{F_{xc}}$ over local exchange [29]

$$\mathbf{U_c^{GGA}}[\mathbf{n_\uparrow(r)}, \mathbf{n_\downarrow(r)}] = \int \mathbf{d^3r\ n(r)F_{xc}}(\mathbf{r_s}, \zeta, \mathbf{S})$$

where $\mathbf{n(r)}$ is the local density at the region $\mathbf{r}$ and $\mathbf{S} = |\nabla \mathbf{n(r)}| / \mathbf{2k_F n}$ is the dimensionless density gradient as was proposed by Perdew-Wang 1986. The enhancement factor was chosen because, it satisfies the uniform scaling condition and recovers the local spin density approximation (LSDA) linear limit for $\mathbf{S} \to \mathbf{0}$. The exchange nonlocality is dominated by valence-electron densities and this has made the GGA to favour density inhomogeneity more than LSD approximation does [29].

3.6 Plane Wave Approach of Density Functional Theory

According to the choice of the basis set for the expansion of the charge densities, valence electrons and potentials, modern electronic structure computation falls into two main broad classes: the plane wave methods or the Gaussian-type orbital methods (i.e, using some kind of localized basis function). The use of plane-waves are considered essential (for studying solids) on account of their immediate advantages which follows from Jürgen Hafer, [38]:

- The simplicity of changing from a real-space representation, where the potential energy is diagonal; through a fast Fourier transformation to a momentum-space representation (a diagonal representation of the kinetic energy).
- Monitoring the eigenvalues and total energy as a function of the cutoff energy (high kinetic energy of the plane wave with the chosen basis set), is adequate. By implication, the control of the basis set convergence is almost considered superficial.

- The stresses acting on the unit cell and the Hellmann and Feynman stress [39] acting on the atoms are calculated in terms of the Hamiltonian with respect to the ionic coordinates. This process is applicable to any particular atom.
- In the plane-wave method, errors due to the superposition of the basis sets are avoided.

In computing the ground state properties of an extended system within the theoretical description of density functional theory, a plane wave approach has become the most widely used. Plane wave approaches are simple and as a result of this, are used as a scheme for solving the Kohn-Sham equations. This is achieved by expanding the single particle eigenstates of the Kohn-Sham into a basis set functions, which leads to the transformation of the Schrödinger equation into a simple matrix eigenvalue problem for the expansion coefficient which may be solved numerically by other well established methods [40]. By definition, plane waves are the exact eigenstates of the homogeneous electron gas. Hence they are a natural basis expansion of the electron wave functions for a simple metals where the ion cores are viewed as small change to the homogeneous electron [41]. Plane waves are orthonormal and energy dependent. It is expedient at this point to ask, why so much emphasis on the plane wave method?

Bloch Theorem

In an infinite crystal the effective potential as well as the electron density, is a periodic function with the periodicity of the lattice, under translational symmetry. The potential being invariant under translation makes the solution of the Kohn-Sham equation repeat itself on the lattice of the crystal. By implication, the solution of the equations in some reduced zone of a system gives the solution of the entire system. We can express the effective potential as

$$\mathbf{V}(\mathbf{r}+\mathbf{T}) \quad = \quad \mathbf{V}(\mathbf{r}), \tag{3.26}$$

where $\mathbf{T}$ is the translational vector given by

$$\mathbf{T} = \mathbf{n_1 a_1} + \mathbf{n_2 a_2} + ... + \mathbf{n_d a_d}. \tag{3.27}$$

$\mathbf{a_i} = \mathbf{1}, ..., \mathbf{d}$ are the primitive translation vectors, $\mathbf{d}$ is the dimension in space and $\mathbf{n_i} = \mathbf{1}, ...\mathbf{d}$ are the integer numbers. In addition, to the translational symmetry of a crystal, are the reflection, inversion and the rotation symmetry that transforms one wave vector into another.

Bloch theorem thus states that, in a periodic solid each electronic wave function can be expressed as the product of a cell-periodic part and a wavelike part [11]

$$\psi_{\mathbf{k}}(\mathbf{r} + \mathbf{T}) = \mathbf{e}^{\mathbf{ikT}}\psi_{\mathbf{k}}(\mathbf{r}). \tag{3.28}$$

$\mathbf{k}$ is the Bloch's wave vector. This theorem affirms that the eigenstates of the translation operators vary from one cell to another in the crystal with the phase factor in equation (3.28). Since the potential $\mathbf{V}(\mathbf{r})$ is periodic in the lattice, the expansion of its plane wave will only contain plane waves with the periodicity of the lattice and wave vectors corresponding exactly to the reciprocal lattice defined by

$$\mathbf{g} = \mathbf{2}\pi(\mathbf{m_1 b_1} + \mathbf{m_2 b_2} + ... + \mathbf{m_d b_d}), \tag{3.29}$$

where the $\mathbf{m_i}$ are integers and $\mathbf{b_i}$ the basis vector of the reciprocal lattice given as $\mathbf{a_i}.\mathbf{b_i} = \delta_{\mathbf{ij}}$ for $\mathbf{k} = \mathbf{g}$. The wave vector $\mathbf{k}$ appearing in Bloch's theorem can always be confined to the first Brillouin zone. It is clearly seen from the above equations, that the periodicity in real space introduces that in the reciprocal space. This means that when considering the electronic structure of solids, it is sufficient to consider the wave vectors contained inside the region of the reciprocal lattice (the Brillouin zone), instead of considering all the vectors [42].

Brillouin Zone Sampling (K-Point sampling)

K-points are wave vectors whose values restrict them to one unit cell of the reciprocal lattice which by convention is referred as the first Brillouin zone (BZ). For a given boundary condi-

tions applicable to a periodic solid, an infinite number of electrons in the solid are accounted for by an infinite number of K-points and only a finite number of electronic states are allowed at each set of K-points. The density of the allowed K-points is dependent on the volume of the solid [40]. This was problematic since such calculation is often long and complicated and thus, in principle requires knowledge of the value of the function at each K-point in the Brillouin zone. The Bloch wavefunction that solves the Kohn-Sham equations have the form

$$\psi_{\mathbf{i}}(\mathbf{r}) \quad = \quad \mathbf{exp(ik.r)f_i(r)}, \tag{3.30}$$

where $\mathbf{f_i(r)}$ is the periodic part of the wavefunction, $\mathbf{i}$ represent the band index. Thus, $\mathbf{f_i(r)}$ can be expanded using the basis set consisting of the plane waves whose wave vectors are the reciprocal lattice vectors of the crystal [42]. It is expressed as: $\mathbf{f_i(r)} = \sum_{\mathbf{G}} \mathbf{c_{i,G} e^{(iG.r)}}$, where $\mathbf{G}$ denote the reciprocal lattice vector. Therefore the plane wave expansion of the wavefunction can be written as

$$\psi_{\mathbf{i}}(\mathbf{r}) \quad = \quad \sum_{\mathbf{G}} \mathbf{c_{i,K+G} e^{i(K+G).r}} \tag{3.31}$$

There are infinite number of k-point in the first Brillouin zone for which the Kohn-Sham Hamiltonian must be solved [43]. The use of Bloch theorem alters the problem of calculating an infinite number of electronic wavefunctions to one of calculating a finite number of eigenstates at an infinite number of K-points. Initially this seems only a minor improvement since an infinite number of calculations are still needed to compute the potential energy contributed by the occupied states at each set of K-points. However, it was possible to represent the wavefunction of a k-space region with the wavefunction at a single k-point. This is because wavefunctions at K-points very close together are almost alike. Hence it was possible to possible to calculate the electronic potential as well as the total energy of a system at the electronic wavefunction of finite K-points. Thus we can replace the integral over the Brillouin zone by a discrete sum:

$$\int_{\mathbf{BZ}} \mathbf{H(K)dK} \quad = \quad \frac{\mathbf{1}}{\mathbf{\Omega}} \sum_{\mathbf{j}} \alpha_{\mathbf{j}} \mathbf{H(k_j)}, \tag{3.32}$$

where $\mathbf{\Omega}$ is the volume of the unit cell at equilibrium, $\mathbf{H}(\mathbf{K})$ is the Fourier transform of $\mathbf{h}(\mathbf{r})$ and $\alpha_{\mathbf{j}}$ (the ratio of the order of the entire point group to the order of the group of wave vector at $\mathbf{k_j}$), is the weight factor associated with $\mathbf{k_j}$ [42]. There are several schemes used in the construction of K-points sampling and these have been proposed in the literature [44, 45, 46]. In this work, we made use of the Monkhorst-Pack mesh [45]. In this scheme, the K-points are evenly distributed throughout the irreducible Brillouin zone (IBZ).

In a practical calculation, K-points are carefully selected to ensure good convergence for the crystal structures to a value better than $\mathbf{1}$meV per atom. The use of dense k-point sampling helps in the calculation of the electronic potential and the total energy in metals, since it defines the Fermi surface precisely.

3.7 Pseudopotentials

The physical and chemical properties of a material are determined by the behaviour of the outer valence electrons of the constituent atoms that make up the bulk solid. The pseudopotential approximation exploits this fact to describe the electron-ion interaction of these bulk materials. The theory is well developed and is interwoven with plane wave method because they allow calculation to be done with a practicable number of plane waves [11].

In practice, plane waves up to a certain cutoff wave vector are only included in the basis set and the convergence calculation with respect to the basis set size controlled by increasing the length of the cutoff wave vector. Nevertheless, a large number of plane waves are needed for good representation of the oscillation due to the nodal structure of the valence wave function in the core region of the atom. In order to make the plane wave method, there is a need to replace the Coulomb potential of the electron-nucleus interaction with a pseudopotential. The introduction of pseudopotential eliminates the need for an explicit description of the strongly bound and chemically inert electron core. Thus, the removal of the core electrons from the calculations implies that total energy differences between ionic

configurations are taken within smaller numbers so that a required accuracy for the total energy calculations can be reached in a short time than it would have when performing the all-electron calculations. Furthermore, by introducing pseudopotentials we are able to replace the true valence wavefunction by a pseudo wavefunction which is expanded using a smaller number of plane wave basis sets. These pseudo wavefunctions are required to be the true valence wavefunction outside the ionic core region but should be nodeless inside the core [40]. Lastly, for a pseudopotential to be useful it has to reproduce the logarithmic derivative of the all-electron potential over a whole range of energy and this makes it transferable to other chemical environments [40].

The use of pseudopotentials have dated back to the work of Fermi [3], in the early 1930s. Although the concept of pseudopotentials had previously existed but they were first understood in terms of the Phillips-Klienman cancellation theorem found in the literature [47]. They argued that the valence wavefunction and the high-energy electron states from the atomic sites should be smooth and oscillate with atomic character in the core region [19]. In general, modern construction of pseudopotential involve solving the all-electron problem for a given atom in a specific configuration (that is, solving the single particle Schrödinger equation within the density function theory in the LDA and GGA approximation). Methods of generating pseudopotential include the norm-conserving pseudopotential [48, 49], the ultrasoft pseudopotentials and the projector augmented plane wave (PAW) method which shall be discussed in this work.

Norm Conserving Pseudopotential

The present day pseudopotentials are not fitted to experiment but are generated from the ab-initio calculation on atomic-like states. The norm conserving pseudopotential concept has contributed greatly to the development of the ab-initio pseudopotential because it simplifies the application of pseudopotential and makes them more transferable and accurate [29]. A good norm conserving potential has to meet a number of requirements given by Hamann *et*

al. [48]. Their potentials are non-local (not simply a function of position) and the potential for each of angular momentum is different. For a norm conserving pseudopotential, the logarithmic derivatives are not only correct at the given energy ε but also correct to linear order for energies $\varepsilon + \mathbf{\Delta}\varepsilon$. This makes the potentials more transferable from the atom to the molecule or solid where the energies change. Thirdly, the all-electron as well as the pseudo valence wavefunction must agree for a representative atomic configuration and finally, the all-electron and the pseudo valence wavefunction must agree beyond a chosen core radius $\mathbf{R_c}$.

From the properties above, to construct a convenient norm conserving pseudopotential, we first do a DFT calculation for the all-electron atomic system to obtain the valence eigenvalues and eigenfunctions for each angular momentum $\mathbf{l}$. We then construct a pseudofunction that is the same outside the core radius $\mathbf{R_c}$ and this is continued smoothly inside the core. To obtain accurate exchange-correlation energy, it is necessary that the pseudo wavefunction and the all-electron wavefunction be identical outside the core region. This means their wavefunctions must be normalized so that both wavefunctions generate identical charge densities

$$\int_{\mathbf{0}}^{\mathbf{R_c}} \psi_{\mathbf{l}}^{\mathbf{AE}} \psi_{\mathbf{l}}^{*\mathbf{AE}} \mathbf{dR} \;=\; \int_{\mathbf{0}}^{\mathbf{R_c}} \psi_{\mathbf{l}}^{\mathbf{PS}} \psi_{\mathbf{l}}^{*\mathbf{PS}} \mathbf{dR}, \tag{3.33}$$

where $\psi_{\mathbf{l}}^{\mathbf{PS}}$ is the pseudo wavefunction with momentum $\mathbf{l}$ and $\psi_{\mathbf{l}}^{\mathbf{AE}}$ is the all-electron wavefunction with momentum $\mathbf{l}$. Equation (3.33) satisfies the norm conserving property. The final step is to find the pseudopotential by inverting the Schrödinger equation

$$\mathbf{V}(\mathbf{r})\psi(\mathbf{r}) \;=\; \varepsilon\psi(\mathbf{r}) + \left(\frac{\hbar^{\mathbf{2}}}{\mathbf{2m}}\right)\left[\frac{\mathbf{2}}{\mathbf{r}}\frac{\mathbf{d}\psi}{\mathbf{dr}} + \frac{\mathbf{d^2}\psi}{\mathbf{dr^2}}\right]. \tag{3.34}$$

This must be done separately for each angular momentum $\mathbf{l}$ [48]. The Figure 3.1 represent the schematic illustration of pseudoelectron, the all-electron potentials and their wavefunction [11] and it gives the pictorial explanation of the equations above.

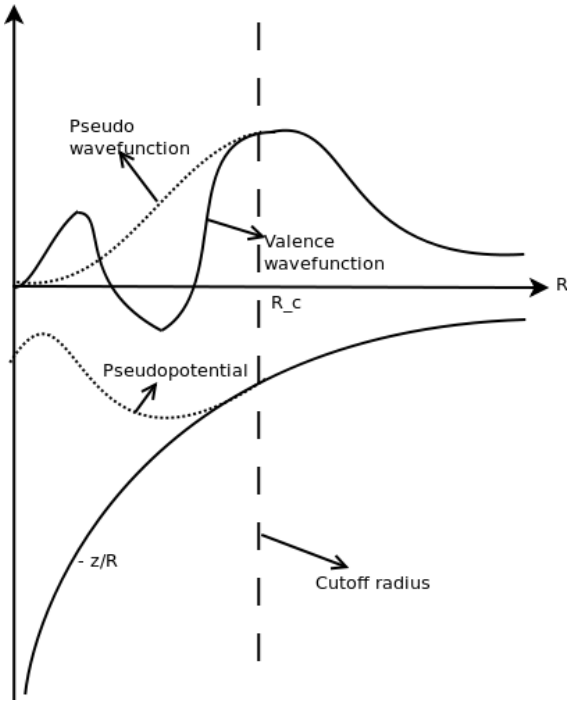


Figure 3.1: The schematic illustration of the pseudoelectron (dashed lines) and the all-electron (solid lines) potentials and their corresponding wavefunctions. $\mathbf{R_c}$ is the radius at which the all-electron and pseudoelectron value match.

Projected Augmented Wave Method (PAW)

The pseudopotential (based on norm-conserving ab-initio pseudopotentials) approach work well for all elements except for the first-row and $3d$ transition metals. It is not able to correctly describe the non-linear core correction required for such systems, where the overlap between valence and core electron densities is not completely negligible. This deficiency is a result of introducing exchange interactions between the valence and core electrons [38]. This led to the introduction of the projected augmented wave (PAW) method by Blöchl [50], followed by the work done in the literature [5].

Projected augmented wave (PAW) method performs electronic structure calculation within the scope of density functional theory. It is known to enhance computational efficiency and

accuracy and also provides the correct wavefunctions, rather than the fictitious wavefunction provided by the pseudopotential approach. The PAW method is more general because it describes the ground state properties (such as the total energy, forces and stress) with an accuracy that compares to its main rival, the full potential linearized augmented plane wave (FLAPW) method and combines it with the pseudopotential method [51]. Unlike the pseudopotential method, the PAW approach encompasses the effects of the nodal features of the valence electronic state which are correctly orthogonalized to the core wavefunctions. Thus, it is referred to as an all-electron (AE) method. Since the method is based on the frozen core (FC), it is however not an all-electron method because all the electronic eigenstates are treated self consistently. This is different from the FLAPW method where the core wavefunctions and charge densities within a spherical approximation to the one-center effective potential, are computed self consistently. The frozen core methods are also used to study the properties of molecules and surfaces.

In detail the PAW method starts from a simple linear transformation that connects the all-electron (AE) valence wave functions $\psi^{\mathbf{AE}}$ to a pseudo (PS) wavefunction $\psi^{\mathbf{PS}}$ which is expanded into a plane wave.

$$\left|\psi^{\mathbf{AE}}\right\rangle = \left|\psi^{\mathbf{PS}}\right\rangle + \sum_{\mathbf{i}} \left(\left|\phi_{\mathbf{i}}^{\mathbf{AE}}\right\rangle - \left|\phi_{\mathbf{i}}^{\mathbf{PS}}\right\rangle\right) \left\langle \mathbf{P}_{\mathbf{i}}^{\mathbf{PS}} | \psi^{\mathbf{PS}} \right\rangle, \tag{3.35}$$

where $\phi^{\mathbf{AE}}$ are the all-electron partial waves which are solutions of the spherical scalar-relativistic Schrödinger equation for an atomic reference energy $\varepsilon_{\mathbf{i}}$ in the valence state is orthogonal to the core states. The $\phi^{\mathbf{PS}}$ are the pseudo partial waves which are nodeless and identical to the AE partial wave outside the core radius. $\mathbf{P}_{\mathbf{i}}^{\mathbf{PS}}$ is the projector function for each pseudo partial wave localized within the augmentation region and satisfies the relation $\left\langle \mathbf{P}_{\mathbf{i}}^{\mathbf{PS}} | \phi_{\mathbf{j}}^{\mathbf{PS}} \right\rangle = \delta_{\mathbf{ij}}$. From equation (3.35), the decomposition of the $\psi^{\mathbf{AE}}$ into three terms holds for wavefunction, kinetic energy, charge densities, Hartree energy and the exchange-correlation energy [50]. In principle, the PAW method is able to recover rigorously the total energy obtained from density functional, if the plane wave and atomic states expansion are complete [38].

3.8 Vienna Ab-initio Simulation Package

The Vienna ab-initio Simulation Package (VASP) [12] code was used in performing almost all the first principle calculations reported in this work. VASP is a plane wave basis set code for ab-initio density functional calculations based on a finite temperature local density approximation or the generalized gradient approximation. The Kohn-Sham ground state equations are solved in a self-consistent cycle with a Pulay optimized charge-mixing routines and the iterative matrix diagonalization scheme [38]. In order to describe the ion-electron interaction, VASP uses the ultra-soft Vanderbilt pseudopotentials (US-PP) or the projected augmented wave (PAW) method. The VASP algorithm calculates the ground state total energy, forces and stress of a given geometry; and from the results obtained elastic and structural properties, relative stability, electronic and magnetic properties can be predicted [12].

4. The Transition Metal Nitrides

The early binary nitrides of transition metals possess an attractive mixture of physical and chemical properties. They constitute a diverse class of materials with interesting technological and fundamental importance because of their strength and durability as well as their optical, electronic and magnetic properties. Often, they are metallic and are used as a barrier layers and contacts [52]. By incorporating any of the light elements, boron (B), carbon (C), nitrogen (N), or oxygen (O) with these transition metals (e.g titanium, vanadium, chromium, zirconium, niobium, hafnium, tantalum and tungsten) compounds with high hardness and compressibility can be synthesized by means of high pressure and high temperature (high P-T) [53, 54].

Recent research has also shown a strong pressure dependence of the oxidation state of metals in these binary compounds, which promises excellent possibilities of discovering novel members of the transition metal nitride group. For the binary nitrides of transition metals, the oxidation states of the cations are limited by a value of +3 even when the available valence electrons is higher [6]. As a result this, most transition metal nitrides: hafnium nitrides (Hf_3N_4), as well as the isomorphic Zr_3N_4 and Ti_3P_4 [55]; Ta_3N_5 [56, 57] and the three noble metal dinitrides PtN_2 [58], IrN_2 and OsN_2 [59] have been synthesized successfully under extreme conditions of pressure and temperature. The large bulk moduli observed experimentally for this class of materials have suggested potential superhard and incompressible solids which could be indispensable for industrial applications and can be used in cutting tools and wear-resistance coatings.

Besides these materials, the most prominent nitrides of group 14 elements having cubic spinel structure (γ-M_3N_4, where M = Si, Ge) have also been synthesized [6]. Many theoretical calculations have been performed to explore their structures since the crystal structure is an important prerequisite of understanding the physical properties of a material. The main interest in these high-pressure binary nitrides is to find materials with enhanced elastic

moduli and hardness. It is likely that these materials will exhibit combinations of fascinating properties which makes them relevant over the existing traditional materials. For example, $\gamma - Si_3N_4$ possesses a high Vickers microhardness, H_v, between $30 - 43$GPa and a high thermal stability in air up to $1673K$ [60, 61], which surpasses that of diamond and cubic boron nitride $(c - BN)$.

In the past decades, the search for nitrides with very high mechanical and chemical properties has been on the increase and this has led to research being extended into the nitrides of tantalum, a group 5 element and their isostructural materials vanadium and niobium.

Recently, binary nitrides of tantalum have become a rapidly growing field of interest with the binary $Ta - N$ system displaying rich compounds with well defined variable stoichiometry [56]. This rich crystal chemistry ranges from solid solutions of nitrogen in tantalum to compounds with $1:1$ composition, several other nitrogen-rich phases (Ta_5N_6 and Ta_4N_5) up to Ta_3N_5, three polymorphs of the mononitride TaN and two phases of Ta_2N [8]. The high pressure $\delta - TaN$ having $NaCl$ structure and the orthorhombic Ta_3N_5 have outstanding properties among the $Ta - N$ phases [56, 6].

From the group of the mononitrides of transition metals, the $\delta - TaN$ has the highest hardness of $30 - 52$GPa and is said to be superconducting [6]. The compound Ta_3N_5 has been shown to be an active photocatalyst material in the visible region of the electromagnetic spectrum and can be used as a red pigment [57]. Henderson *et al.* [57] synthesized nanocrystalline Ta_3N_5 using the ammonolysis of amorphous Ta_2O_5 power. Their result show an aggregate product with oxygen persistent in it even after the reaction time was extended. The ab-initio band structure calculation performed by Fang *et al.*[62] was found to be 2.08eV, which makes Ta_3N_5 a potential substitute for the toxic chalcogenides in various optoelectronic applications.

4.1 Tantalum Nitrides

Ta_3N_5 is composed of irregular TaN_6 octahedra with both three and four coordinate of nitrogen atoms and has the pseudobrookite (Fe_2TiO_5) structure which was confirmed by Brese and O'Keeffe [63] using powder neutron diffraction. Kroll *et al.*[56] predicted the existence of the high pressure Ta_3N_5 having a high bulk modulus of 378GPa at pressure greater than 9GPa through the first principle calculation and the results are in good agreement with the experimental work carried out by Henderson and Hector [57].

Cubic TaN_x having fluorite, CaF_2 structure was also reported [8]. According to X-ray and electron diffraction data, the compound crystallizes in the cubic $c - Ln_2O_3$ structure type (space group no. 206 ($Ia\bar{3}$), f.u = 16), an ordered defect $2 \times 2 \times 2$ superstructure of the fluorite type. As a result of the analogy to the well-known bixbyite ($c - Ln_2O_3$- type), the authors postulated the stoichiometry to be Ta_2N_3 adopting the bixbyite phase.

However, the details of the real structure regarding the precise position of the nitrogen atom was not wholly determined. Due to the relatively uncertainty in the nitrogen position, a model structure was introduced which allows a nitrogen position equidistant from the tantalum neighbour to be calculated for each value of $Ta(2)$. The resulting bond length of the $Ta - N$ was found to be $2.109\mathring{A}$. All of these extension of research of nitride of group 5 elements, led to the discovery of the novel tantalum nitride, Ta_2N_3 with an orthorhombic U_2S_3 structure [6].

Very recently, Zerr *et al.*[6] synthesized the novel tantalum nitride having an orthorhombic U_2S_3 structure (space group $Pbnm$ (62), $a = 8.19\mathring{A}, b = 8.18\mathring{A}, c = 2.98\mathring{A}$, f.u = 4) using the Kawai- type multi-anvil apparatus at high pressure and temperature conditions. With the aim of obtaining the high pressure phase predicted by Kroll *et al.*[56], orthorhombic Ta_3N_5 was used as starting material. The composition of this sample was observed to have changed during the high pressure and temperature synthesis according to this equation,

$$2Ta_3N_5 \longrightarrow 3Ta_2N_3 + 0.5N_2.$$

This novel tantalum nitride is considered the first thermodynamic stable transition binary nitride having an anion-cation ratio that exceeds 4 : 3. The tantalum (cations) and the nitrogen (anions) in the unit cell of the nitride were both subjected to a mirror plane transformation, in wyckoff position of $4c(x, y, 1/4)$. This is to prevent the mirror plane from generating short interatomic spacing as a result of the small lattice parameter c. From the experimental findings of Zerr *et al.*[6], orthorhombic Ta_2N_3 display high hardness and a unique texture and this makes it a potential candidate of a hard and fracture resistant material for industry.

As part of this dissertation, we perform a detailed investigation of the elastic and mechanical properties of the novel tantalum nitride and then we extend our work to the nitrides of Vanadium (V) and Niobium (Nb). We also calculate the electronic band structure, the density of state (DOS) and the relative stability of the ternary phases of the nitrides at zero-pressure and temperature.

5. Elastic, Structural, Electronic and Relative Stability Properties of the Orthorhombic Metal Nitrides of Tantalum, Vanadium and Niobium

The ability to accurately predict the ground state properties (equilibrium volume, elastic properties, electronic band structure, density of states and relative stability) of a material, is the purpose of electronic structure methods. Elastic properties are the properties of a material that undergoes stress, deforms and then recovers and returns to its original state after the removal of stress [64]. These properties are obtained from the ground state total energy calculations and are very important because they have a correlation with the basic solid state properties such as equation of state and phonon spectra. They are said to be linked thermodynamically to the specific heat, thermal expansion, Debye temperature and melting point [65].

In order to treat the elastic properties of the orthorhombic metal nitrides, we computed the total energy of the systems from first principle rather than rely upon any assumptions on the nature of the interatomic forces. We present the underlying theory behind the calculation of the equilibrium properties of the orthorhombic metal nitrides.

5.1 Elasticity of the Orthorhombic Metal nitride

The response of a crystal to an external force (stiffness), is determined by the elastic constants. The values of the elastic constants obtained from the ground state total energy calculation, contain vital information about the bonding characteristic between adjacent

atomic planes, structural stability and the anisotropic character of the bonding. The elastic constants are characterized by the bulk modulus, Young's modulus, shear modulus and Poisson's ratio, and so play a vital role in determining the strength of a material [66]. A typical hard material requires a high bulk modulus (for the material to support the volume decrease created by the applied force), and a low Poisson's ratio or high shear modulus such that the material will not deform in a direction different from that of the external force.

The estimation of the elastic constants of a material from first principles is very demanding. It not only requires accurate methods for calculating the total energy but also involves intensive computation. For example, if the symmetry of the system is reduced, the number of independent moduli increases and hence a large number of distortions are required to calculate the full set of elastic constants. For a completely asymmetric material, the elastic behaviour is specified by 21 independent elastic constants whereas, for an isotropic material, the number is 2. In between these limits, the number necessary is determined by the symmetry of the material [64]. In an orthorhombic crystal, there are nine independent elastic constants and theses are usually referred to as $C_{11}, C_{12}, C_{13}, C_{23}, C_{22}, C_{33}, C_{44}, C_{55}$, and C_{66} [65]. These can be deduced by applying small strain to the equilibrium lattice position and determining the change in the total energy. Another important factor beside the calculation of the elastic constants, is the investigation of the lattice stability. This was originally carried out by Born *et al.*[67], who showed that by expanding the internal crystal energy as a power series in the strain and by imposing the convexity of the energy, it is possible to obtain a stability requirement in terms of a set of conditions involving the elastic constants [68]. There are stability criteria for other crystal symmetries but our focus are those of the orthorhombic crystal. The requirement of mechanical stability for orthorhombic crystals with nine elastic constants are as follows [68]:

$$(C_{11} + C_{22} - 2C_{12}) > 0, (C_{11} + C_{33} - 2C_{13}) > 0, (C_{22} + C_{33} - 2C_{23}) > 0,$$
$$C_{11} > 0, C_{22} > 0, C_{33} > 0, C_{44} >, C_{55} > 0, C_{66} > 0,$$

and

$$(C_{11} + C_{22} + C_{33} + 2C_{12} + 2C_{13} + 2C_{23}) > 0. \tag{5.1}$$

5.2 Calculation of the Isotropic Moduli

A first principle method that employs periodic boundary conditions assumes the existence of a single crystal, which means that we can directly compare the calculated elastic constants obtained to any available experimental data for single crystals. However, in the absence of such data, the polycrystalline bulk B, and shear G moduli can be determined [66]. The Voigt and the Ruess methods are the two approximations used in determining the values of the bulk and the shear moduli [65]. A detailed review of the Voigt-Ruess methods can be found in the literature[69]. In the calculation of the average isotropic elastic crystals from the anisotropic single crystal elastic constants, it is observed that the Voigt and Ruess assumption results in the theoretical maximum and minimum values of the isotropic elastic moduli respectively. In this work, we utilized the Voigt method in the calculation of the elastic moduli. For orthorhombic lattices, the Voigt bulk and shear are given as:

$$B = \frac{1}{9}(C_{11} + C_{22} + C_{33}) + \frac{2}{9}(C_{12} + C_{13} + C_{23})$$

and

$$G = \frac{1}{15}(C_{11} + C_{22} + C_{33} - C_{12} - C_{13} - C_{23}) + \frac{1}{5}(C_{44} + C_{55} + C_{66})$$

The Young's modulus E and Poisson's ratio ν are the other two elastic constants that describes the hardness of an isotropic material. They are expressed as

$$E = \frac{9BG}{3B + G} \qquad and \qquad \nu = \frac{3B - 2G}{2(3B + G)}$$

Another vital parameter that enhances the understanding of the behaviour (such as the ductility or the brittleness) of an isotropic material, is the quotient of bulk to shear modulus

(B/G) of polycrystalline phase. This was introduced by Pugh [70]. Considering that the bulk modulus B to represent the resistance to fracture and the shear modulus G to represent resistance to plastic deformation, he suggested the critical value that separates the ductile and brittle character of a material to be about 1.75. The values for which B/G is greater than 1.75 indicates the ductile character of the material while for values of B/G less than 1.75, the material display brittle features.

In all, the most important physical property is the material's hardness. This is related to compressibility as measured by the bulk modulus and the shear modulus [71].

5.3 The Equation of State

The equation of state (EOS) is fundamentally relevant in the understanding of a solid. It is dependent on the nature of their interatomic interactions and as such is used in predicting the thermodynamic properties such as the pressure-volume and temperature relation. For theoretical analysis of the equation of state, the total energy E which is expressed as a function of volume (V) at zero-temperature, is most convenient because it is easier to carry out electronic structure calculations at fixed volume. In essence, volume is considered a vital parameter that can be used to study a system theoretically [29].

To describe the equation of state effectively, several approaches have been put in place which include the stress-strain and the energetics relation of the solid. This approach has been relatively successful in finding fitting forms such as the Murnaghan equation [72], the Birch-Murnaghan equation [73], the Vinet universal equation [74] and the Birch equation of state [75]. In this work, we employed the first order Birch equation of state, since it depends on the finite elastic strain of the solid. This equation of state is also in a good agreement with the equations of Murnaghan [74]. The Birch EOS can be expressed as

$$E_B(V) = \frac{9}{16} B_0 V_0 \left(\frac{B_0' - 4}{X^2} - B_0' + 6 \right) \left(\frac{1}{X^2} - 1 \right)^2 + E(V_0). \tag{5.2}$$

where

$$X = \left(\frac{V}{V_0}\right)^{\frac{1}{3}}.$$

and V_0 represents the isothermal volume, B_0 the isothermal bulk modulus, B_0' the pressure derivative of the bulk and the equilibrium energy of the material is denoted as $E(V_0)$. We define the bulk modulus of the material as;

$$B_0 = -V_0\frac{dP}{dV}.$$

Thus, pressure is defined as the negative gradient of the total equilibrium energy and the volume i.e.,

$$P = -\frac{dE}{dV}.$$

Therefore, the isothermal bulk modulus can then be rewritten as;

$$B_0 = V_0\frac{d^2E}{dV^2}.$$

This shows the bulk modulus as effectively measuring the curvature or the second derivative of the energy versus volume relation at the relaxed volume V_0. In calculating the equation of state, the first step is to determine theoretically the equilibrium volume V_0, where energy E is minimum (i.e $P = 0$), and the bulk modulus B_0 of the crystal structure at zero-pressure.

Since V_0 and B_0 requires to be extrapolated at zero-temperature, it becomes a rigorous test for the theory. Therefore we followed a procedure that requires us to calculate the equilibrium energy E for several values of the volume. These was achieved by varying the scaling factor in the lattice structure and the data generated was fitted into the analytic equation (5.2). This gave the predicted values for the equilibrium volume per atom, V_0, the equilibrium energy per atom E_0, the bulk modulus B_0 and the pressure derivative of the bulk modulus, B_0'. The results are presented in the latter part of this work.

5.4 Results Analysis

In this section, we report detailed first principle calculations of the structural and electronic properties of the advanced metal nitrides, M_2N_3 (where $M = Ta, V$ and Nb) and their ternary phases in the orthorhombic U_2S_3 structure. Furthermore, we access the relative stability of the alloys of the metals nitrides with respect to their constituent mixtures. Before, we present our results, the details of the computational method used in this work are shown below.

5.4.1 Computational Analysis

The electronic structures describing the pseudopotential of the atoms that are of interest are as follows: $Ta : 5p^6 6s^2 5d^3$; $V : 3p^6 3d^4 4s^1$; $Nb : 4p^6 5s^2 4d^5$ and $N : 2s^2 2p^3$. In this work, we performed the zero-pressure and temperature ab-initio calculations of the optimized geometries and the elastic properties of the metal nitrides, as well as the relative stability of their alloys. Calculations were performed within the framework of the density functional theory as implemented in the Vienna ab-initio Simulation package (VASP) [12]. The plane wave formalism using the local density approximation (LDA) by Ceperley-Alder [36], parameterized by Perdew and Zunger [35]; and the generalized gradient approximation (GGA-PBE), parameterized by Perdew *el at.*[76] treats the exchange-correlation potentials. The geometry relaxation, total energy calculation and all derived quantities were obtained using first principle projector augmented wave method [5, 4]. The Kohn-Sham orbitals were expanded using a plane wave cutoff energy of 400eV or 500eV in order to calculate the optimized geometries, elastic constants, electronic properties and the relative stability of the advanced metal nitrides. For accurate Brillouin zone integration, we use the special K-point sampling with a $8 \times 8 \times 8$ Monkhorst-pack meshes, resulting in 64 K-points in the irreducible part centered at Γ [45].

Before a full first principle computation can be done on any material, it is important to

ensure that the total energy converges in terms of the expansion of the wave function, charge density and potentials. For good convergence, it is necessary and sufficient to choose K-point sampling in the Brillouin zone in order to ensure that all structures are well converged to better than 1meV per atom. For the advanced metal nitrides and their ternary phases, we carried out calculation involving relaxation of their structural parameters (atomic position and lattice parameters) using the $12\times12\times12$ and the $8\times8\times8$ Monkhorst-Pack meshes. The convergence with respect to the energy cutoff for $8\times8\times8$ mesh was between 0.4meV/atom and 0.9meV/atom for the different structures. For the $12\times12\times12$ mesh calculations, the convergence was worse. The total energy calculation allows one to decide the stability of a system. Therefore the system with low equilibrium energy is said to be stable. The $8\times8\times8$ mesh calculations gave a much lower equilibrium energy than those of the $12\times12\times12$ mesh. This test showed that the K-point sampling ($8\times8\times8$) we used is adequate.

A full geometry optimization was performed on each of the metal nitrides system with all atoms relaxing as their cell structure changes. For the calculation of the elastic constants, we applied an external strain to the crystal (within the elastic limit) and by calculating the curvature of the total energy as a function of strain, the nine elastic constants for each of the orthorhombic metal nitrides and their ternary phases were obtained. With the constraint of constant volume, we repeated optimization of the materials several times in order to obtain a set of total energies as a function of cell volume. From this, the equilibrium volume and bulk modulus were obtained by a fit to a first order Birch equation of state given in equation (5.2). These results were compared with the ones obtained from the elastics constants.

5.4.2 Cell Parameters of the Metal Nitrides

The search for the most stable structure of the newly synthesized Ta_2N_3 [6], has prompted the consideration of the orthorhombic U_2S_3 structure of the advanced metal nitrides M_2N_3 with a $M:N$ stoichiometry of 3 : 4 having a space group of **pbnm** (number 62). To start with, we considered the 20-atom (formula unit, $Z=4$) unit cell which is common to all

the metal nitrides and their ternary phases. We used the cell parameters and fractional coordinates of Ta_2N_3 for every other metal nitride (the V_2N_3 and Nb_2N_3) considered in this work. Table 5.1 and 5.2 explicitly shows the LDA and the GGA values (in parenthesis), of the optimized calculated structural parameters for the binary metal nitrides as well as their ternary phases at a plane wave energy cutoff of 400eV and the 500eV, respectively. The experimental and the theoretical values of Ta_2N_3 are also presented for comparison. The calculated lattice parameters at an energy cutoff of 400eV exhibit similar trends with those obtained from energy cutoff of 500eV indicating that the choice of plane wave cutoff is acceptable. It is evident that the values of the lattice parameters of each material was underestimated and slightly overestimated by the LDA and the GGA respectively. This is consistent with what one expect from LDA and GGA [77].

For the orthorhombic Ta_2N_3, our results (the lattice parameters) are in agreement with experiment [6] and a recent theoretical calculation [7] which employed the all-electron projector augmented wave method within the generalized gradient approximation of Perdew et al.[76]. The lattice parameters (a, b, and c) of the orthorhombic Ta_2N_3 are bigger than the experimental values by about 1% respectively. We also calculated the total energy of Ta_2N_3 as a function of volume and our theoretical equilibrium volume, $193.43\mathring{A}^3$ is within 3.0% of the experimental volume [6].

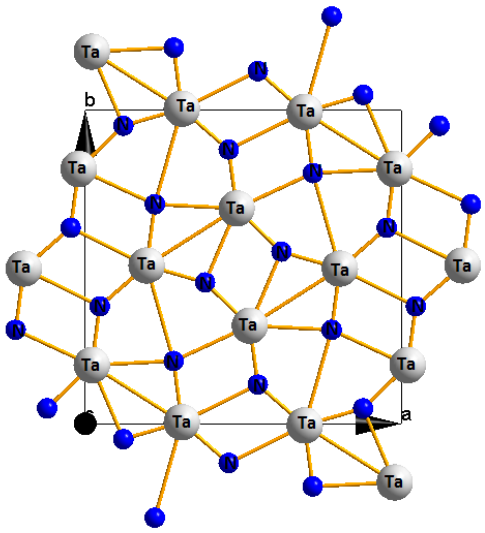
Table 5.1: The calculated LDA and the GGA values of the equilibrium cell structures (Å)of the metal nitrides and their ternary phases at plane wave energy cutoff of 400eV.

Samples	a	b	c	Reference
Ta_2N_3	8.129 (8.206)	8.036 (8.129)	2.961 (2.990)	This work
V_2N_3	7.633 (7.744)	7.540 (7.677)	2.749 (2.791)	This work
Nb_2N_3	8.191 (8.271)	8.007 (8.135)	2.980 (3.005)	This work
$TaVN_3$	7.948 (8.080)	7.588 (7.716)	2.888 (2.930)	This work
TaV_3N_6	7.797 (7.923)	7.542 (7.691)	2.828 (2.872)	This work
Ta_3VN_6	8.021 (8.135)	7.843 (7.982)	2.917 (2.959)	This work
$NbTaN_3$	8.152 (8.246)	7.967 (8.110)	2.983 (3.014)	This work
$NbTa_3N_6$	8.132 (8.220)	7.978 (8.162)	2.968 (2.999)	This work
Nb_3TaN_6	8.175 (8.260)	7.984 (8.150)	2.982 (3.008)	This work

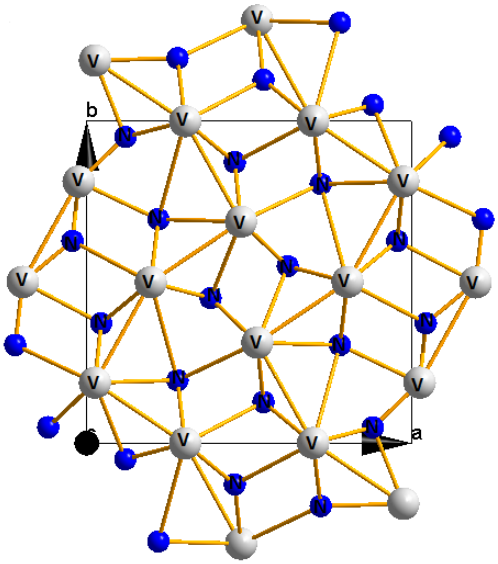
Figures 5.1 and 5.2 show the schematic representation of the three binary metal nitrides and their ternary phases. From the Figures, each metal atom is bonded by five closely packed nitrogen atoms , so it is concluded that the size of the lattice parameters of the metal nitrides are determined mainly by the size of the metal atoms. There is an evident of structural difference between Ta_2N_3 and V_2N_3. Although the reason for this difference is not yet clear, it is likely related to the extent at which electron correlates at high volume in the two different structures. The equilibrium volume of V_2N_3 is about 18.0% smaller than that of Ta_2N_3 whereas, that of Nb_2N_3 is about 2.0% larger than that of Ta_2N_3.

Table 5.2: Calculated LDA and the GGA values of the equilibrium cell structures (Å)of the metal nitrides with space group Pbnm and their ternary phases at plane wave energy cutoff of 500eV.

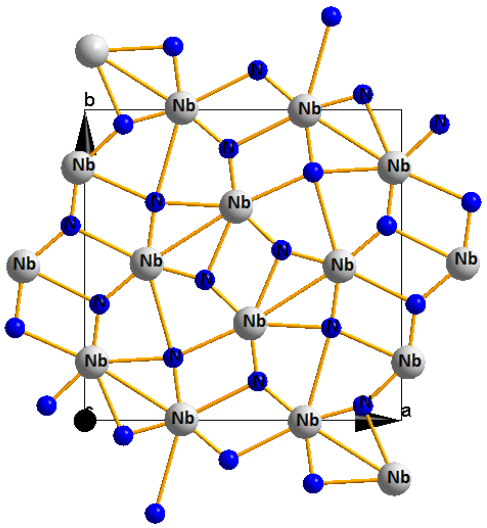
Samples	a	b	c	Reference
Ta_2N_3	8.129 (8.236)	8.036 (8.185)	2.961 (3.002)	This work
	8.19	8.18	2.98	[6]
	(8.19)	(8.24)	(3.00)	[7]
V_2N_3	7.633 (7.758)	7.540 (7.706)	2.749 (2.795)	This work
Nb_2N_3	8.224 (8.310)	8.042 (8.189)	2.992 (3.020)	This work
$TaVN_3$	7.976 (8.116)	7.597 (7.726)	2.895 (2.939)	This work
TaV_3N_6	7.816 (7.944)	7.552 (7.701)	2.834 (2.878)	This work
Ta_3VN_6	8.045 (8.164)	7.870 (8.015)	2.925 (2.969)	This work
$NbTaN_3$	8.176 (8.274)	8.000 (8.149)	2.995 (3.027)	This work
$NbTa_3N_6$	8.154 (8.242)	8.014 (8.214)	2.978 (3.009)	This work
Nb_3TaN_6	8.201 (8.286)	8.021 (8.205)	2.994 (3.018)	This work



(a) Ta_2N_3

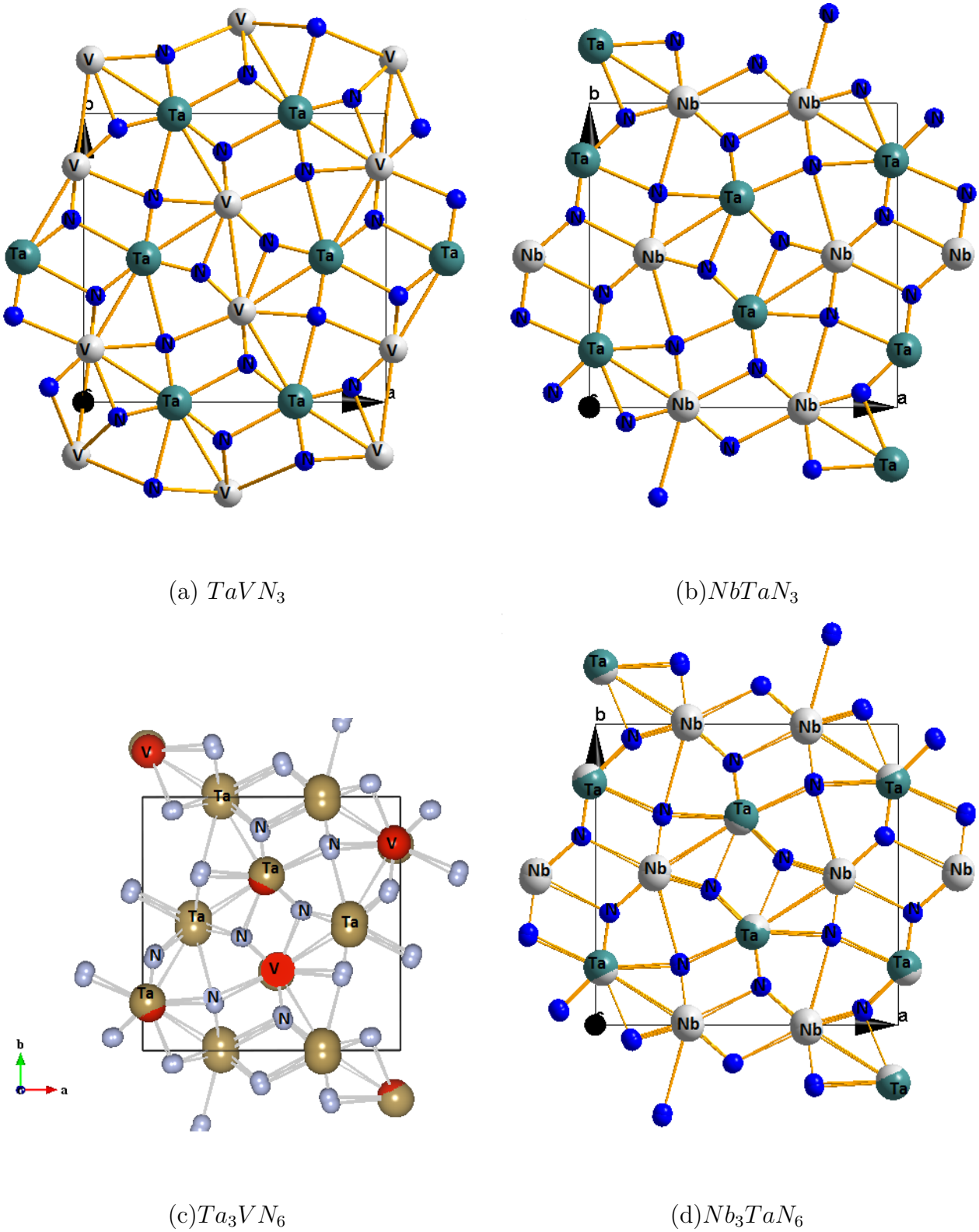


(b)V_2N_3



(c)Nb_2N_3

Figure 5.1: Crystal structures of the binary metal nitrides with U_2S_3 structure.



(a) $TaVN_3$ (b)$NbTaN_3$

(c)Ta_3VN_6 (d)Nb_3TaN_6

Figure 5.2: Crystal structures of the ternary metal nitrides with U_2S_3 structure.

5.4.3 Structural Properties Calculation

Structural properties of the metal nitrides and their ternary phases are examined by first principle calculations at zero pressure-temperature. The total energy as a function of volume was then fitted to the first order Birch equation of state (EOS) described in section 5.3. The assumption employed for this equation of state is that near equilibrium relaxed state the bulk modulus varies linearly with the pressure and no phase transition occurs during the compression of the material. Our calculated LDA and GGA values of zero-pressure energy, equilibrium volume V_0, bulk moduli B_0 and the pressure derivatives of the bulk B_0' at plane wave energy cutoffs of 400eV and 500eV are summarize in Tables 5.3 and 5.4, with GGA values in parenthesis. The previous theoretical result of the bulk modulus and the pressure derivative are also presented in Table 5.4 for comparison. From the results shown in these Tables, the bulk modulus B_0' obtained from the LDA calculations are much higher than those of the GGA calculations because, GGA typically under-estimates bulk modulus with respect to LDA [77]. The calculated pressure derivatives B_0', of each of the samples are within the range of $4-5$ which is common for most solids. The bulk modulus B_0' and the pressure derivative of the bulk B_0' of the Ta_2N_3 are in agreement with the recent theoretical result [7]. The bulk modulus results also shows that the binary and the ternary metal nitrides could be potential hard materials when compared to that of diamond, except for the GGA value obtained for TaV_3N_6.

Table 5.3: Calculated LDA and GGA values of the equilibrium structural properties and relative stability energies at plane wave energy cutoff of 400eV.

Samples	E_{tot} (eV/atom)	B_0' (GPa)	B'	V_0 ($\mathring{A}^3$/atom)	ΔE_{stab} (eV/atom)
Ta_2N_3	-11.864 (-10.775)	372 (326)	4.404 (4.607)	9.676 (10.132)	
V_2N_3	-10.276 (-9.230)	354 (300)	4.503 (4.455)	7.912 (8.366)	
Nb_2N_3	-10.971 (-9.868)	334 (302)	4.563 (4.706)	9.900 (10.292)	
$TaVN_3$	-11.113 (-10.046)	365 (316)	4.421 (4.531)	8.773 (9.225)	-0.229 (-0.263)
TaV_3N_6	-10.671 (-9.618)	351 (295)	4.686 (4.873)	8.365 (8.830)	-0.00005 (-0.078)
Ta_3VN_6	-11.488 (-10.414)	363 (318)	4.434 (4.563)	9.265 (9.722)	-0.227 (-0.347)
$NbTaN_3$	-11.430 (-10.326)	352 (314)	4.504 (4.606)	9.797 (10.214)	-0.073 (-0.093)
$NbTa_3N_6$	-11.647 (-10.553)	362 (312)	4.498 (4.738)	9.733 (10.194)	-0.085 (-0.177)
Nb_3TaN_6	-11.201 (-10.099)	343 (300)	4.522 (4.923)	9.849 (10.268)	-0.091 (-0.179)

Table 5.4: Calculated LDA and GGA values of the equilibrium structural properties and relative stability energies at plane wave energy cutoff of 500eV.

Samples	E_{tot} (eV/atom)	B_0' (GPa)	B'	V_0 ($\AA^3$/atom)	ΔE_{stab} (eV/atom)
Ta_2N_3	−11.862 (−10.774)	370 (326)	4.435 (4.522)	9.676 (10.130)	
		(323)	(4.45)	[7]	
V_2N_3	−10.275 (−9.231)	355 (302)	4.468 (4.630)	7.913 (8.358)	
Nb_2N_3	−10.970 (−9.867)	335 (303)	4.479 (4.634)	9.903 (10.290)	
$TaVN_3$	−11.112 (−10.045)	364 (315)	4.482 (4.645)	8.772 (9.216)	−0.215 (−0.220)
TaV_3N_6	−10.670 (−9.617)	352 (295)	4.672 (5.104)	8.363 (8.819)	0.020 (−0.017)
Ta_3VN_6	−11.487 (−10.413)	362 (317)	4.432 (4.545)	9.264 (9.716)	−0.212 (−0.260)
$NbTaN_3$	−11.429 (−10.325)	352 (315)	4.435 (4.576)	9.798 (10.210)	−0.065 (−0.030)
$NbTa_3N_6$	−11.646 (−10.552)	362 (313)	4.427 (4.643)	9.735 (10.191)	−0.068 (−0.057)
Nb_3TaN_6	−11.200 (−10.098)	343 (300)	4.457 (4.838)	9.851 (10.267)	−0.073 (−0.055)

5.4.4 Calculated Elastic Properties

Using the ab-initio approach at plane wave energy cutoff of 400eV and 500eV we obtained all the elastic constants and thereafter, we estimated the effective Voigt isotropic moduli (bulk modulus B, shear modulus G and the Young modulus Y), the Poisson's ratio and the ratio of B/G for each of the metal nitrides M_2N_3 and their ternary phases. These results are listed in Tables 5.5- 5.8. The elastic constants obtained satisfy the mechanical stability criteria stated in equation (5.1) indicating the orthorhombic **pbnm** structures are mechanically stable. Plane wave energy cutoffs need to be sufficiently large to ensure accurate computation of stress tensor related quantities like elastic properties and also for good convergence. From the results, we observed a progressive decrease in the values of the elastic constants, bulk, shear and Young modulus of the metal nitrides of tantalum, vanadium and niobium as the energy

cutoff increases from 400 to 500eV, and this was especially notable for the GGA values. Bulk modulus is the resistance to volume change (that is, the inverse of compressibility), and from Tables 5.5 and 5.6 we can see that the order of compressibility from high to low is $Nb_2N_3 > V_2N_3 > Ta_2N_3$ for the binary metal nitrides. This means that Ta_2N_3 is the lowest compressible material among the binary metal nitrides. The comparison from the ternary phases shows that low concentrations of vanadium and niobium are most significant and promising improvement of the Ta_2N_3. The requirement for a material with high bulk moduli is that C_{11} must be high with C_{12} low [13]. Of all the materials considered, as can be seen from Figure 5.3, the LDA and GGA trends shows Ta_2N_3 as having the highest bulk modulus because of it high value of C_{11} but this does not imply that in all the planes that its elastic constants are higher than the rest of the binary and ternary metal nitrides. The higher the shear strength (C_{44} value), the higher the stiffening of the lattice plane of the material. This means that the elastic constants C_{ij} are relatively high in all the planes of that material and this explains why the shear modulus value of Ta_2N_3 is small as compared to that of V_2N_3. For the ternary phases, our calculations show an increasing trend in bulk modulus, shear modulus and the Young's modulus when using both the LDA and GGA. One exception is for TaV_3N_6 where the GGA values of the shear and Young's moduli; 118 GPa and 314 GPa as can be seen clearly from Figure 5.3. These low values can be attributed to incomplete convergence of the total energy and thus, we suggest future work to be conducted. All the binary and ternary metal nitrides exhibit a ductile character since their B/G values are all greater than the 1.75. In comparison to diamond and cubic boron nitride, the binary and ternary metal nitrides could be regarded as potential hard materials because of their increasing trends in bulk modulus.

Table 5.5: The LDA calculated values of the elastic constants and the Voigt isotropic moduli (the bulk modulus B, shear modulus G, Young modulus Y) in GPa, Poisson's ratio ν and the quotient of B/G. The experimental data for diamond are $G = 544$GPa, $B = 442$GPa, $Y = 1142$GPa and $\nu = 0.1$. Calculation were performed at a plane wave energy cutoff of 400eV.

Samples	C_{11}	C_{12}	C_{13}	C_{23}	C_{22}	C_{33}	C_{44}	C_{55}	C_{66}	B	G	Y	ν	B/G
Ta_2N_3	771	312	225	262	572	779	125	249	222	413	207	533	0.29	2.00
V_2N_3	719	313	204	249	545	764	228	232	210	395	218	553	0.27	1.81
Nb_2N_3	683	288	104	92	516	455	161	213	200	291	193	474	0.23	1.51
$TaVN_3$	672	292	229	229	664	812	188	246	233	405	227	573	0.26	1.78
TaV_3N_6	681	296	218	232	599	776	146	234	221	394	208	530	0.28	1.89
Ta_3VN_6	710	315	219	242	577	803	164	242	215	405	212	541	0.28	1.91
$NbTaN_3$	713	307	212	248	581	724	191	229	213	395	210	535	0.27	1.88
$NbTa_3N_6$	738	308	213	256	574	742	169	240	218	401	210	537	0.28	1.91
Nb_3TaN_6	703	300	207	241	560	703	181	220	206	384	203	517	0.28	1.89

Table 5.6: The LDA calculated values of the elastic constants and the Voigt isotropic moduli (the bulk modulus B, shear modulus G, Young modulus Y) in GPa, Poisson's ratio ν and the quotient of B/G. The experimental data for diamond are $G = 544$GPa, $B = 442$GPa, $Y = 1142$GPa and $\nu = 0.1$. Calculation were performed at a plane wave energy cutoff of 500eV.

Samples	C_{11}	C_{12}	C_{13}	C_{23}	C_{22}	C_{33}	C_{44}	C_{55}	C_{66}	B	G	Y	ν	B/G
Ta_2N_3	700	288	204	239	507	710	85	225	197	375	181	467	0.29	2.07
V_2N_3	655	295	186	231	484	703	205	209	186	363	195	497	0.27	1.86
Nb_2N_3	606	265	185	221	445	631	135	187	177	336	167	430	0.29	2.01
$TaVN_3$	605	273	209	209	603	746	163	220	210	371	203	515	0.27	1.83
TaV_3N_6	616	277	198	214	538	712	120	210	197	360	184	472	0.28	1.96
Ta_3VN_6	642	291	198	219	517	737	141	217	192	368	189	485	0.28	1.95
$NbTaN_3$	647	282	192	221	508	658	166	204	190	356	187	477	0.28	1.90
$NbTa_3N_6$	666	283	194	238	510	686	140	215	195	366	187	478	0.28	1.96
Nb_3TaN_6	633	275	187	216	491	641	155	195	184	347	179	459	0.28	1.94

Table 5.7: The GGA calculated values of the elastic constants and the Voigt isotropic moduli (the bulk modulus B, shear modulus G, Young modulus Y) in GPa, Poisson's ratio ν and the quotient of B/G. The experimental data for diamond are $G = 544$GPa, $B = 442$GPa, $Y = 1144$GPa and $\nu = 0.1$. Calculation were performed at a plane wave energy cutoff 400eV.

Samples	C_{11}	C_{12}	C_{13}	C_{23}	C_{22}	C_{33}	C_{44}	C_{55}	C_{66}	B	G	Y	ν	B/G
Ta_2N_3	690	280	201	233	513	710	45	220	194	371	172	446	0.30	2.15
V_2N_3	612	275	176	214	479	683	202	197	179	345	190	481	0.27	1.82
Nb_2N_3	630	270	194	222	486	652	116	199	180	349	171	441	0.29	2.04
$TaVN_3$	590	258	199	199	577	733	154	209	200	357	196	496	0.27	1.82
TaV_3N_6	585	258	187	203	495	693	-19	198	189	341	149	489	0.31	2.29
Ta_3VN_6	627	276	191	207	530	730	141	209	185	359	188	480	0.28	1.91
$NbTaN_3$	645	277	190	224	513	662	126	206	187	356	179	460	0.28	1.99
$NbTa_3N_6$	657	266	190	227	483	692	209	209	178	355	196	496	0.27	1.81
Nb_3TaN_6	628	261	189	230	438	659	197	198	176	343	184	468	0.27	1.86

Table 5.8: The GGA calculated values of the elastic constants and the Voigt isotropic moduli (the bulk modulus B, shear modulus G, Young modulus Y) in GPa, Poisson's ratio ν and the quotient of B/G. The experimental data for diamond are $G = 544$GPa, $B = 442$GPa, $Y = 1144$GPa and $\nu = 0.1$. Calculation were performed at a plane wave energy cutoff of 500eV.

Samples	C_{11}	C_{12}	C_{13}	C_{23}	C_{22}	C_{33}	C_{44}	C_{55}	C_{66}	B	G	Y	ν	B/G
Ta_2N_3	613	253	179	208	443	639	−43	193	166	331	133	353	0.32	2.49
Ta_2N_3*	456	248	203	176	610	639	165	193	−54	327	132	350	0.32	2.47
V_2N_3	543	251	157	194	409	619	177	172	154	308	165	420	0.27	1.87
Nb_2N_3	551	243	171	197	416	582	78	171	154	308	143	372	0.30	2.15
$TaVN_3$	519	237	181	183	513	667	128	183	179	322	171	437	0.27	1.88
TaV_3N_6	522	241	169	185	432	632	−80	174	165	308	118	314	0.33	2.61
Ta_3VN_6	557	252	171	184	468	663	119	184	162	323	165	423	0.28	1.96
$NbTaN_3$	573	254	170	202	447	596	90	181	164	319	153	396	0.29	2.08
$NbTa_3N_6$	586	242	168	198	429	629	186	183	153	318	173	440	0.27	1.84
Nb_3TaN_6	554	237	165	196	406	600	174	172	150	306	163	416	0.27	1.88

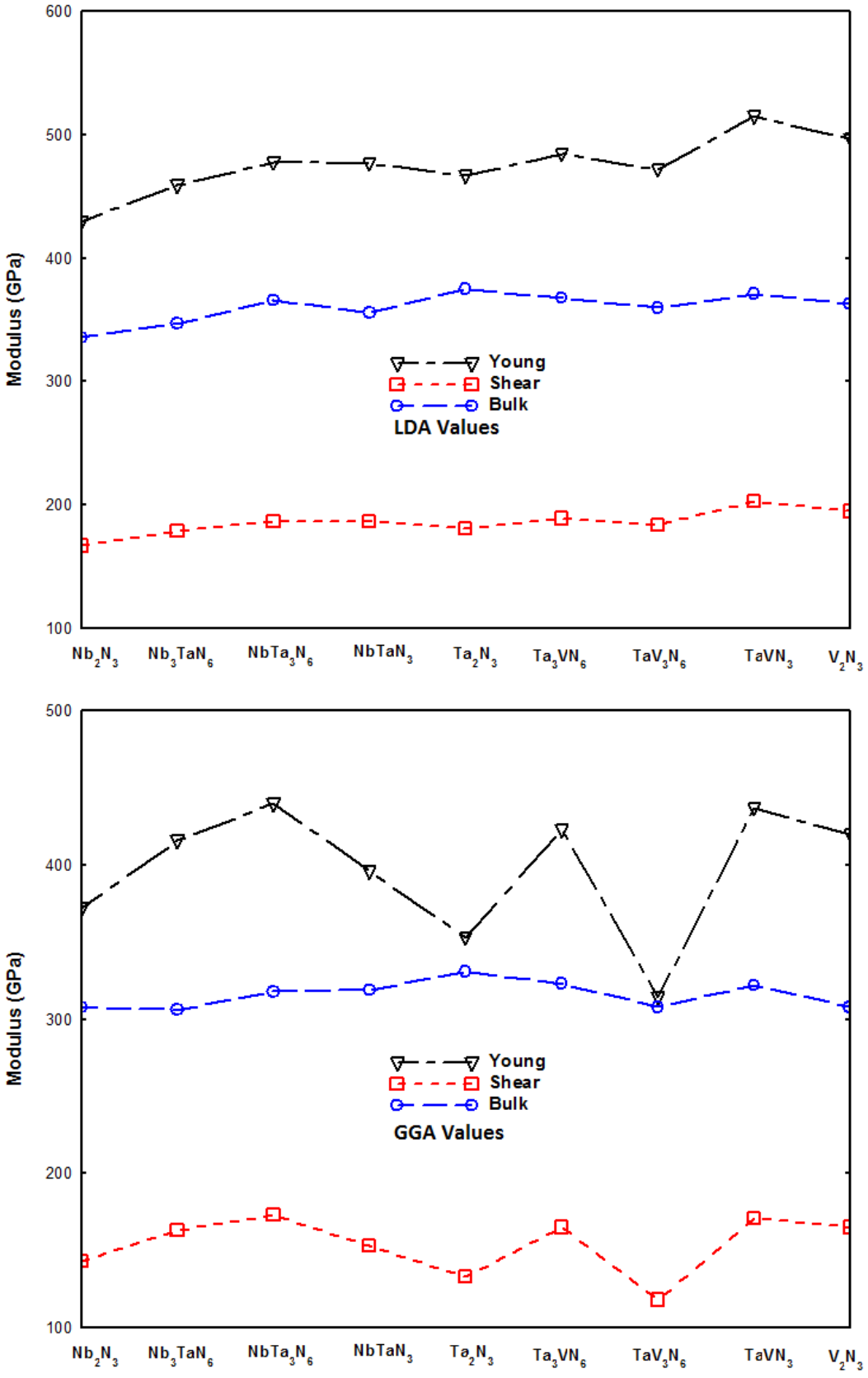


Figure 5.3: The isotropic bulk properties (LDA and the GGA values) of the binary metal nitrides and their ternary phases at plane wave energy cutoff of 500eV.

5.4.5 Relative Stability

The relative stability of an alloy is the measure of the difference between the total energy of the bulk material at equilibrium and the total energy of the constituent phases at zero-pressure and temperature. Each of these energies are the total energy of the optimized structure considered. For this work, we considered the relative stability of the advanced metal nitrides, M_2N_3 with respect to the mixture of each of the starting materials (namely Ta_2N_3, V_2N_3 and Nb_2N_3). Scaling factors (the reaction concentrations) of the reaction were emphasized due to their importance when computing relative stability. In the absence of application of extreme conditions of temperature and pressure, the reaction energy utilized in this work is expressed as:

$$\Delta E_{stab} = E_{tot}(M_X M_Y N_Z) - \left[\frac{tE_{tot}(M_2N_3) + pE_{tot}(M_2N_3)}{2}\right].$$

Depending on the reacting constituents, M can either represent Nb and Ta or Ta and V. X and Y can alternatively take the value 1 or 3, while Z can take the value 3 or 6. E_{tot} denotes the total energy of the optimized geometry and corresponds to the free energy at zero temperature and pressure, p and t represents the reaction concentration (or ratio) and ΔE_{stab} indicates the relative stability of the ternary phase. We carried out this computation using both the local density approximation (LDA) and the generalized gradient approximation (GGA). The implication of this definition is that if ΔE_{stab} is positive the two constituent phases are not miscible (i.e, it is meta stable) and if ΔE_{stab} is negative the phases are miscible (i.e, it is stable) [71]. It is not just enough to be strongly miscible, but for an alloy to be more stable than another, it must have a certain range of bond strength [78].

Our calculated relative stability both, the LDA and the GGA for the different ternary phases are listed in Tables 5.3 and 5.4. These data are represented more clearly in Figures 5.4 and 5.5 below. These figures show a stable bahaviour for most of the $Nb - Ta - N$ systems at both energy cutoffs. The $Ta - V - N$ trends shows a stable characteristic at both cutoffs except TaV_3N_6 which displays a meta-stable character. Figures 5.4 and 5.5 also suggest

more bond strength in Ta_3VN_6 and Nb_3TaN_6 than all the other ternary phases.

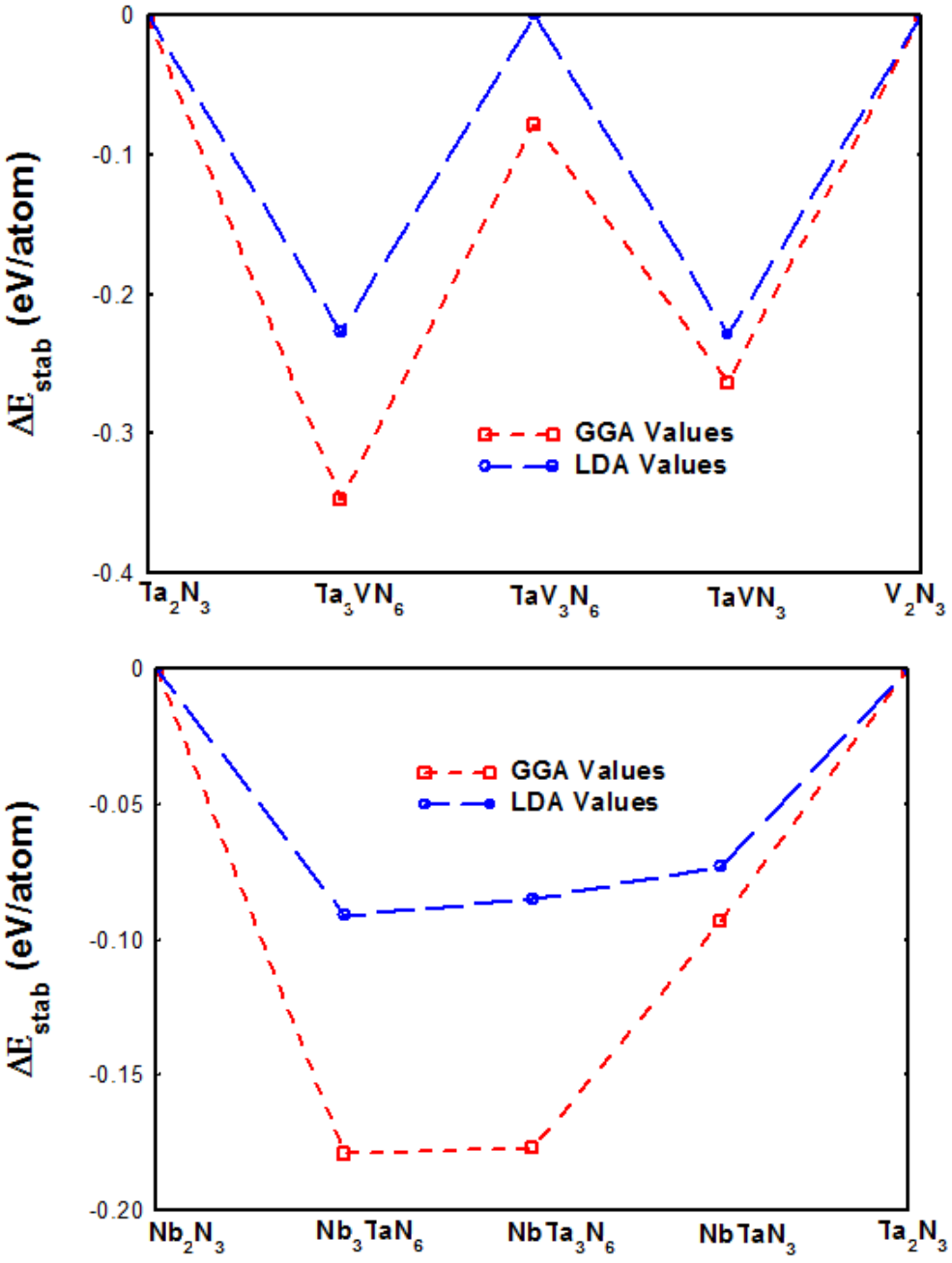


Figure 5.4: The relative stability (LDA and GGA values) of the ternary phases of the metal nitrides in $Ta-V-N$ and $Nb-Ta-N$ trends at energy cutoff 400eV.

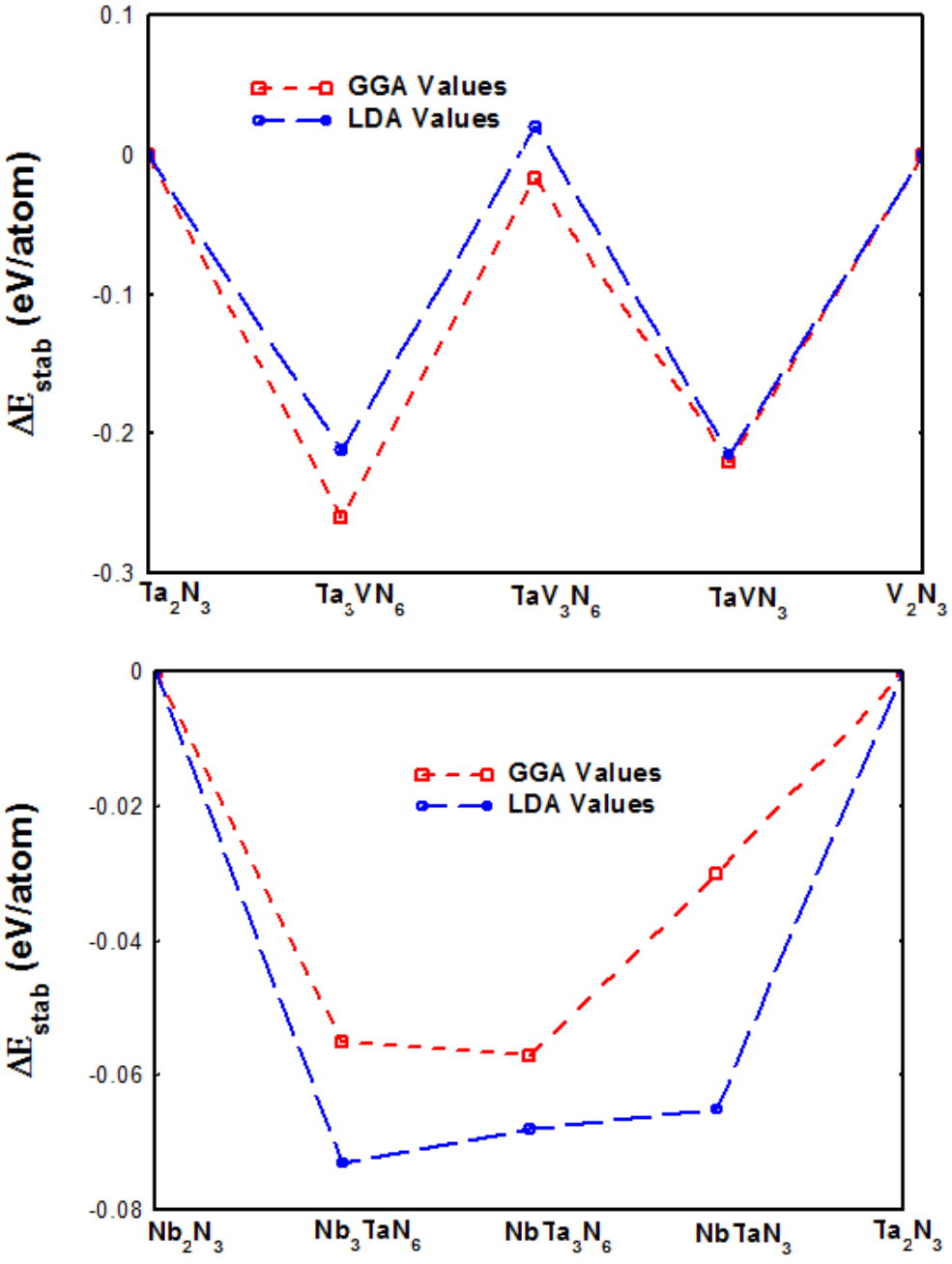


Figure 5.5: The relative stability (LDA and GGA values) of the ternary phases of the metal nitrides in $Ta-V-N$ and $Nb-Ta-N$ trends at energy cutoff 500eV.

5.5 Electronic Structure Calculation

Electronic properties (like the band structure, density of states and the charge density distribution) of a material provides valuable information on the distribution of the states in k-space. A good interpretation of the electronic states has helped in the understanding of the structural stability and various other physical properties quantitatively [79].

In order to understand the electronic nature of the advanced metal nitrides, M_2N_3 and their ternary phases, we have computed their band structures, the density of states (DOS), and the electron density. In the reduced Brillouin zone, the Hamiltonian was solved self-consistently at $8 \times 8 \times 8$ special K-points of the orthorhombic unit cell. To evaluate the band structure and density of states, we used the Monkhorst-pack interpolation scheme along some high symmetry lines in the Brillouin zone of the orthorhombic system as shown in the figure 5.6 [80] below. We also used the FP-LAPW method as employed in the WIEN2k code [81] to determine the band structures of Ta_2N_3, V_2N_3, Nb_3TaN_6 and Ta_3VN_3. The recent non-empirical GGA approach of Wu and Cohen [82] has been considered. To ensure sufficient accuracy in convergence, the total energy of the crystal was converged to 0.01 mRy. Energy-eigenvalue convergence was achieved by expanding the wave functions in the interstitial region into plane waves with a cut-off wave vector $Kmax = 9/R_{MT}$, where R_{MT} denotes the smallest atomic sphere radius and the $Kmax$ is maximal reciprocal lattice vector. The valence wave functions inside the spheres are expanded up to $lmax = 10$, while the charge density was Fourier-expanded up to $Gmax = 12$. The Brillouin zone integration was performed for 250 points.

The energy band structures, total density of states and the charge densities of the advanced metal nitrides M_2N_3 and their ternary phases are shown in Figure 5.7 - 5.16, respectively. The energy band structure yields the whole picture of electron spectrum of these metal nitrides and the plots depicts the formation of a hole-like structure near the Fermi surface and the overlap of these bands confirm metallic behaviour of the metal nitrides. Their lower

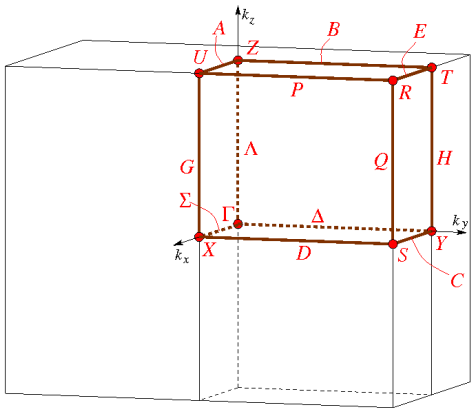


Figure 5.6: The Brillouin zone of the orthorhombic unit cell with points of high symmetry indicated.

valence bands are mainly occupied by the $2s$-states of the N atoms whereas the top valence band and the bottom of the conduction band are composed of N $2p$ states and the d-states from the transition metal. The results from VASP and WIEN2K basically depict the same interpretation.

From Figure 5.12, with the Fermi level (E_f) set as 0eV, we observed that all the advanced metal nitrides are metallic because of the finite DOS at the Fermi level (E_f). The plots for the total DOS also show the presence of a deep valley-pseudogap, very close to the Fermi level. In the metal nitrides M_2N_3, the presence of narrow d-states near the E_f pulled towards lower energy range from Fermi level due to resonance effect and therefore causing deep valley near the E_f to appear. This pseudogap causes a separation between the bonding and the antibonding states [83] which results in the strong hybridization between d-states in the metals and the $N-2p$ states. A material has high stability if the conduction band is narrow or if conduction electron states accumulate in the relatively lower energy region. From the Figures 5.12- 5.14, the advanced metal nitrides are expected to be structurally stable. All the DOS of the metal nitrides have very similar topography in that, the peak found in the lower energy region between -13eV and -17eV is dominated by the $2s$ states of N. In addition,

the total DOS below (E_f) for all the transition metal nitrides is mainly dominated by the N $2p$ states in the region 0eV to -8.0eV, which is consistent with the higher electronegativity of N atoms relative to the transition metals. This is justified by the fact that the localization of electrons in N atoms are stronger than that of the transition metals, despite the presence of strong hybridization between N and the other transition metals. The DOS values at the Fermi level [N(E_f)] for the binary metal nitrides are $11.0, 8.80$ and 9.0 states/eV for V_2N_3, Ta_2N_3 and Nb_2N_3, respectively.

The charge density distribution gives information about the changes in the bond type and the charge transfer in a material. To further understand the changes of the DOS at the Fermi energy level, we calculated the charge density of the advanced metal nitrides. The plots are shown in Figure 5.15 and 5.16. The plots of the charge density shows an evident of directional bonds between the metals and the nitrogen. These bonds are not so strong since the localization of electrons in N atoms are stronger than that of the transition metals and hence, seems to improve the ductility of the metal nitrides.

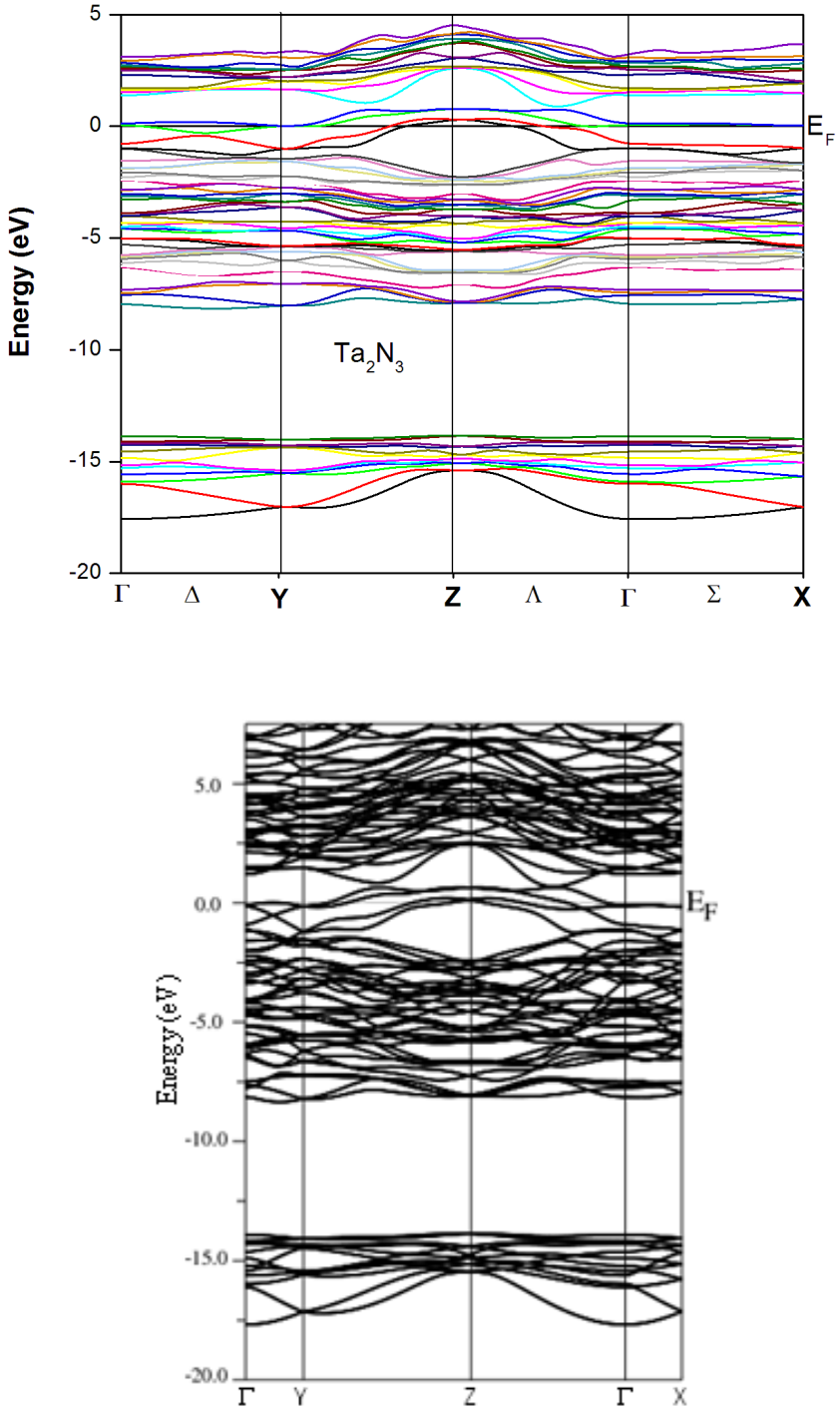


Figure 5.7: Electronic band structure for Ta_2N_3 using both VASP and WIEN2K (at the bottom). The Fermi energy level is set at 0 eV.

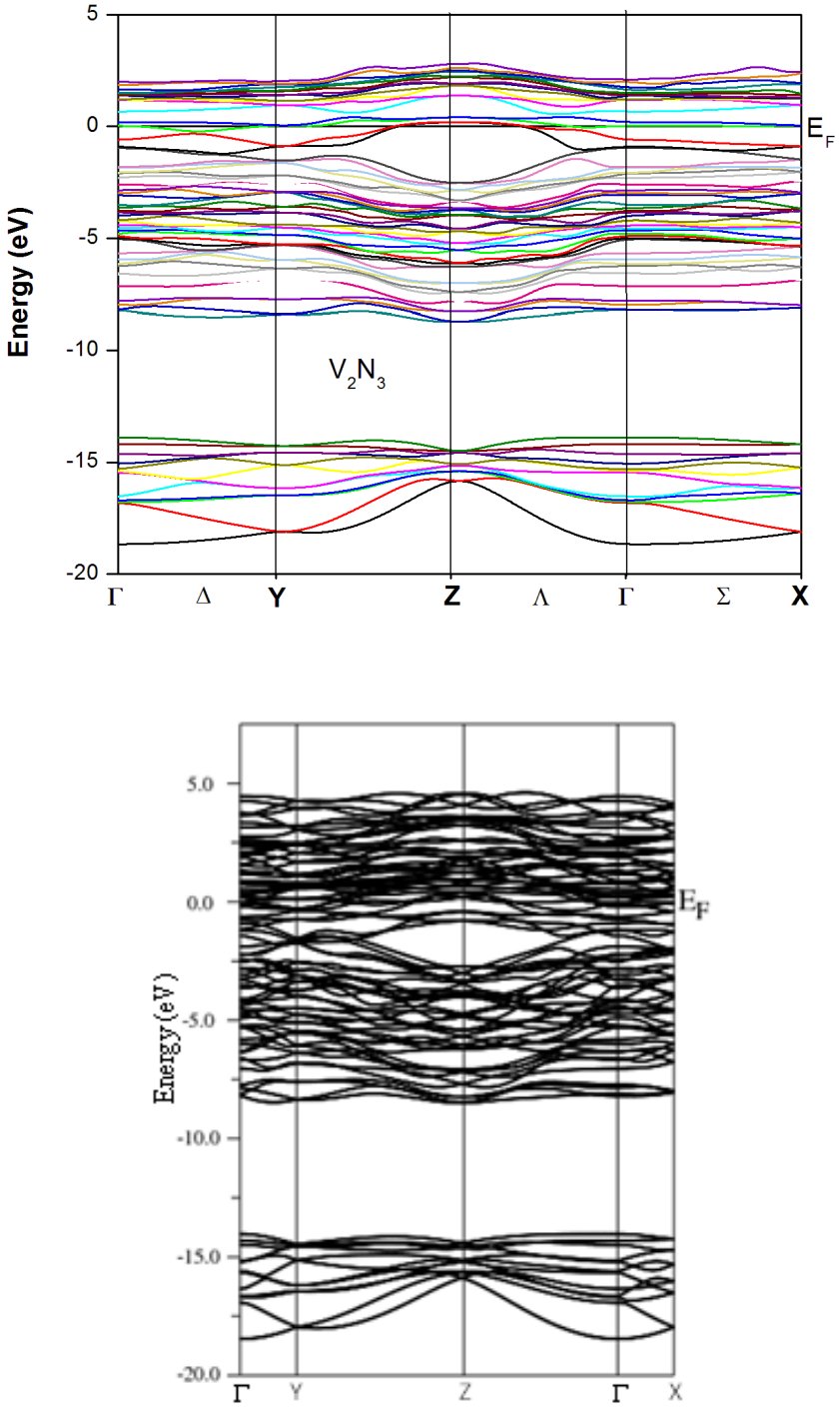


Figure 5.8: Electronic band structure for V_2N_3 using both VASP and WIEN2K (at the bottom). The Fermi energy level is set at 0 eV.

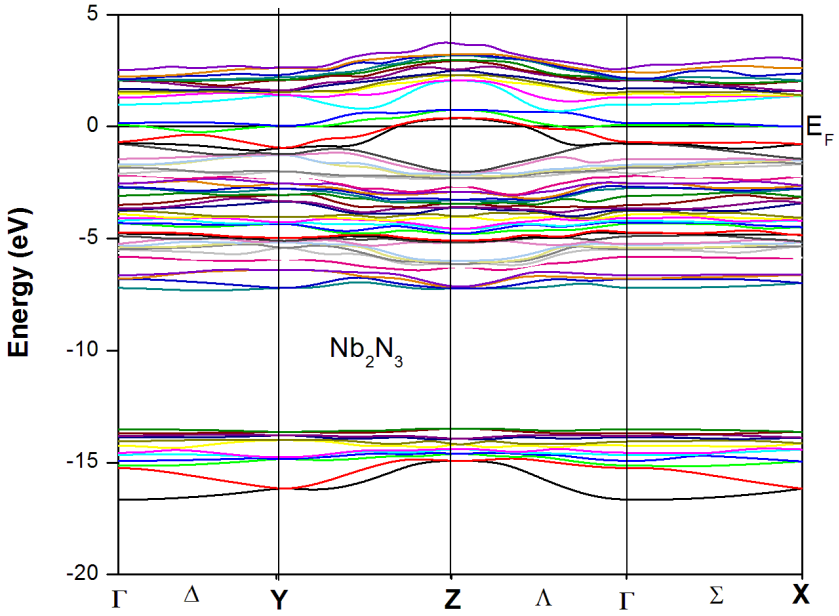


Figure 5.9: Calculated electronic band structure for Nb_2N_3 using VASP. The Fermi energy level is set at 0 eV.

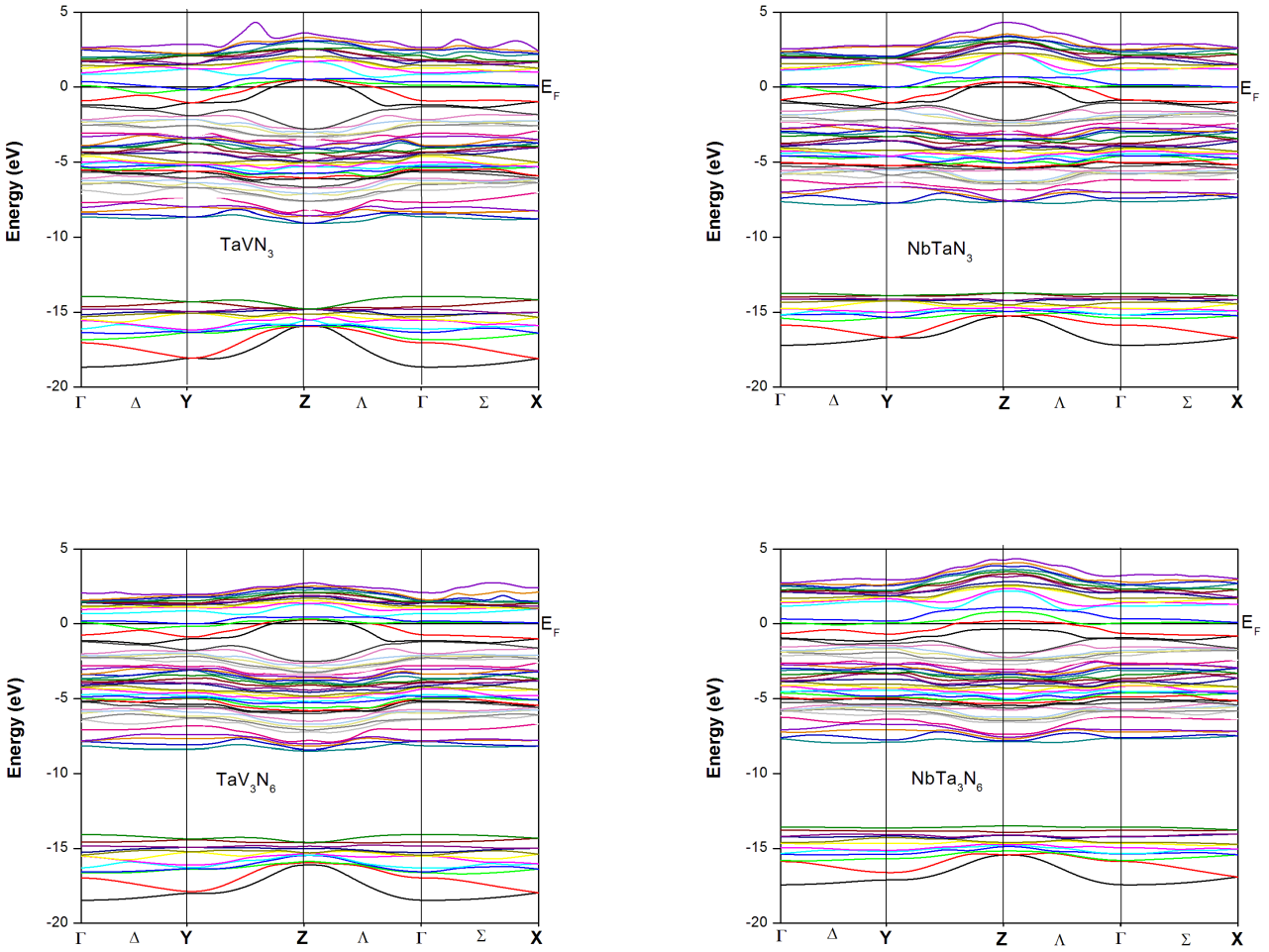
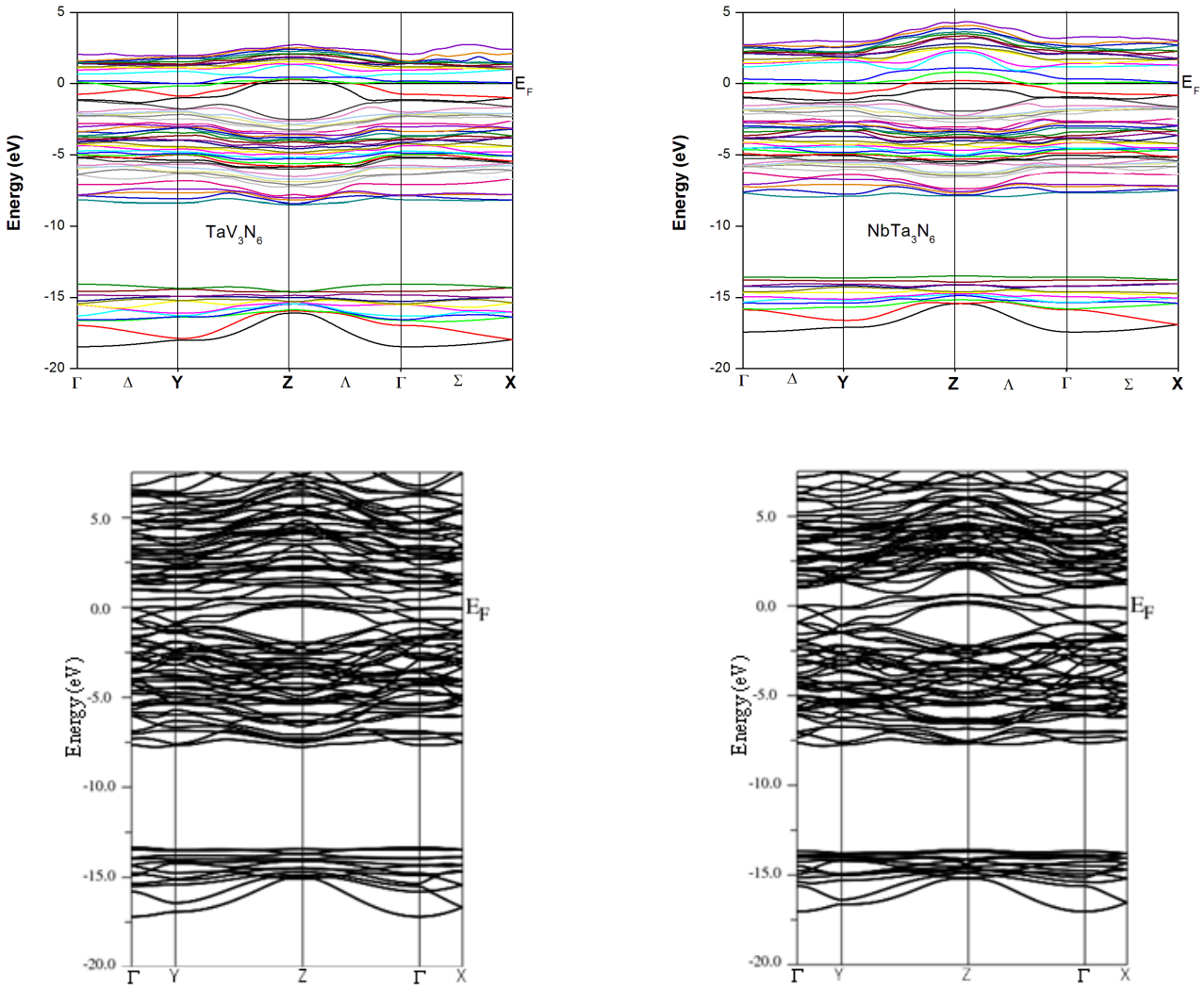


Figure 5.10: Electronic band structure for the ternary metal nitrides. The Fermi energy level is set at 0 eV.



Ta_3VN_6 Nb_3TaN_6

Figure 5.11: Electronic band structure for the ternary metal nitrides. The Fermi energy level is set at 0 eV. (The WIEN2K results at the bottom).

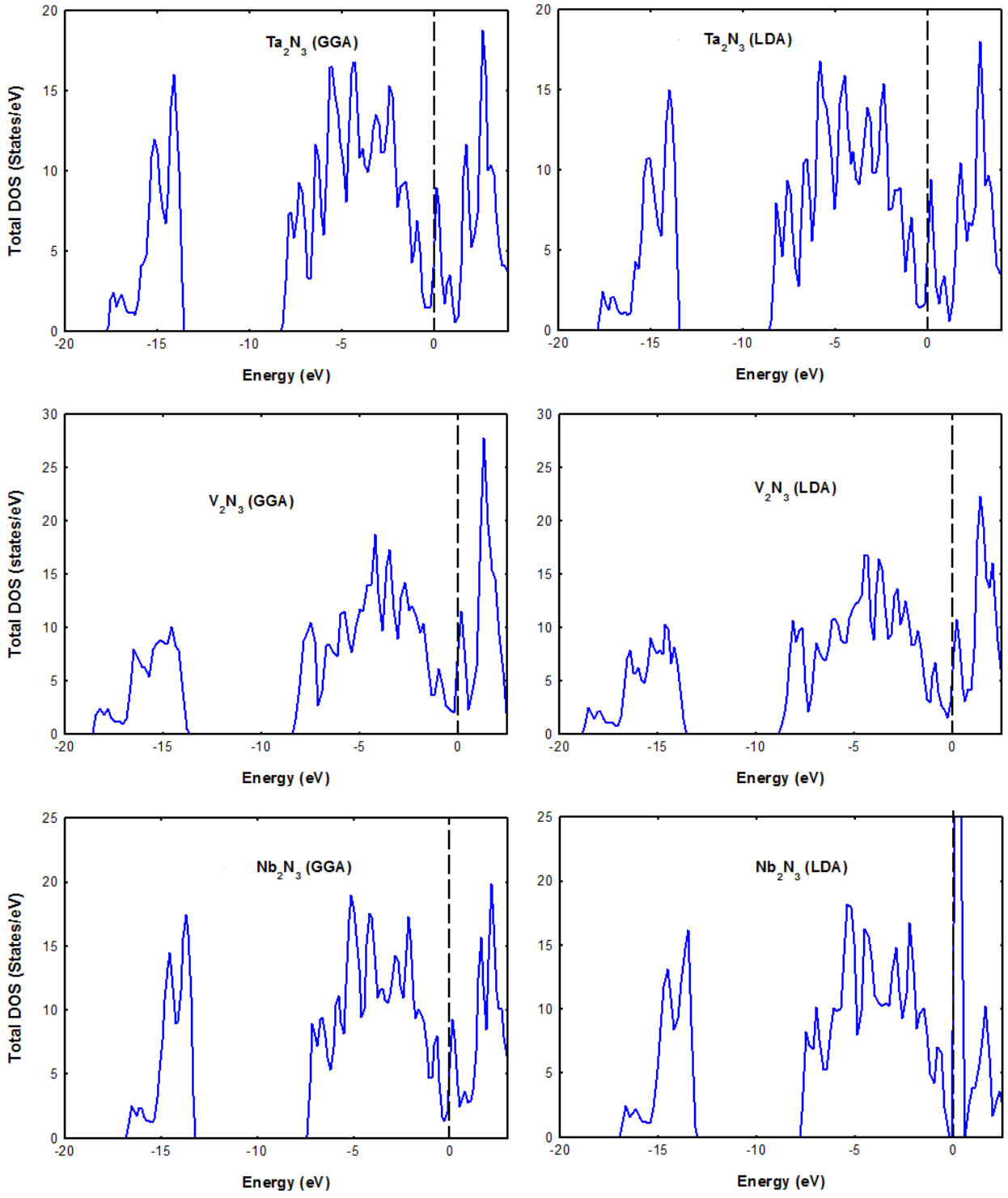


Figure 5.12: The plots of the total density of states (DOS) of the binary metal nitrides. The Fermi level is set at 0 eV and is indicated as a dashline.

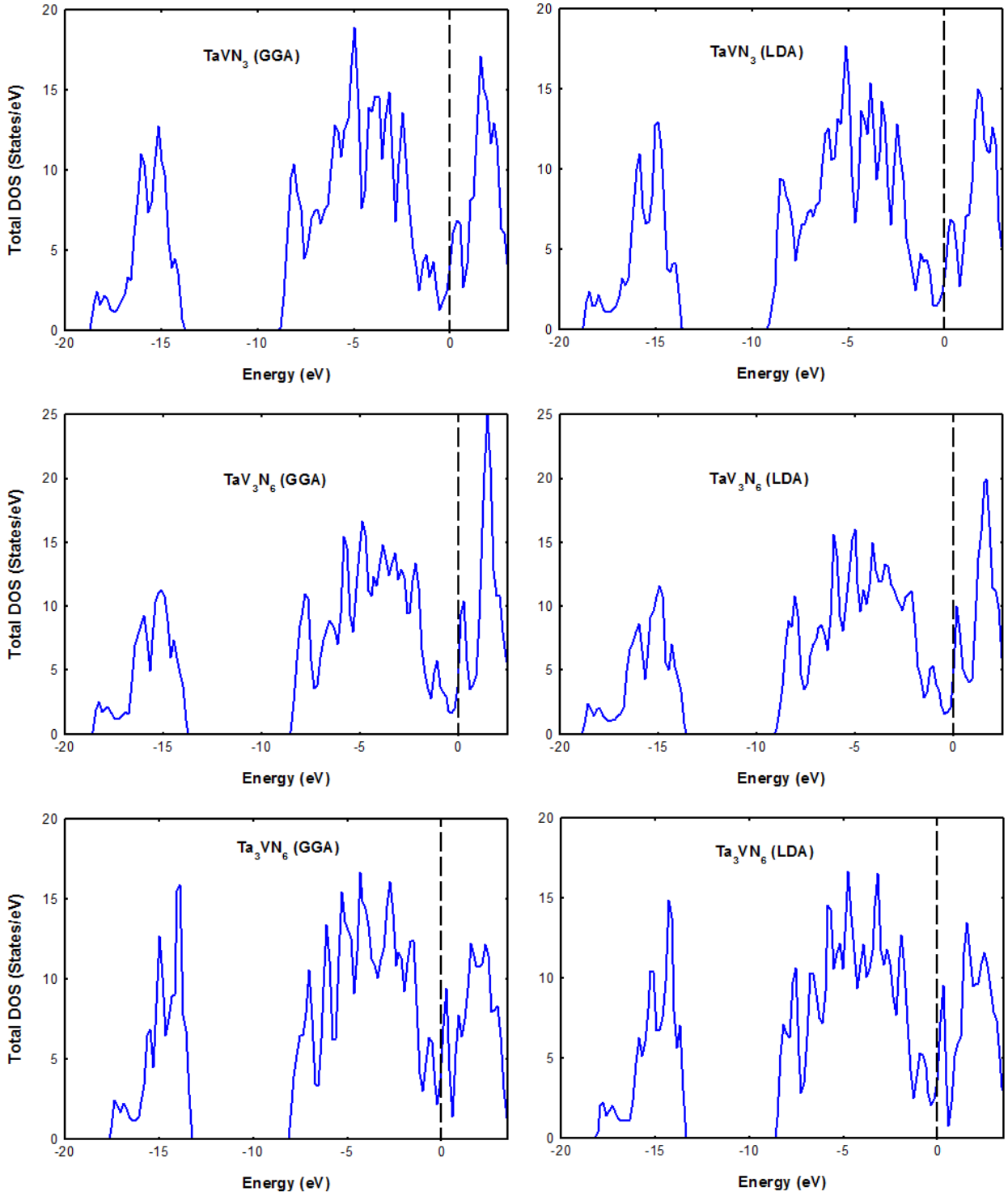


Figure 5.13: The plots of the total density of states of the ternary phases of the metal nitrides. The Fermi level is set at 0 eV and is indicated as a dashline.

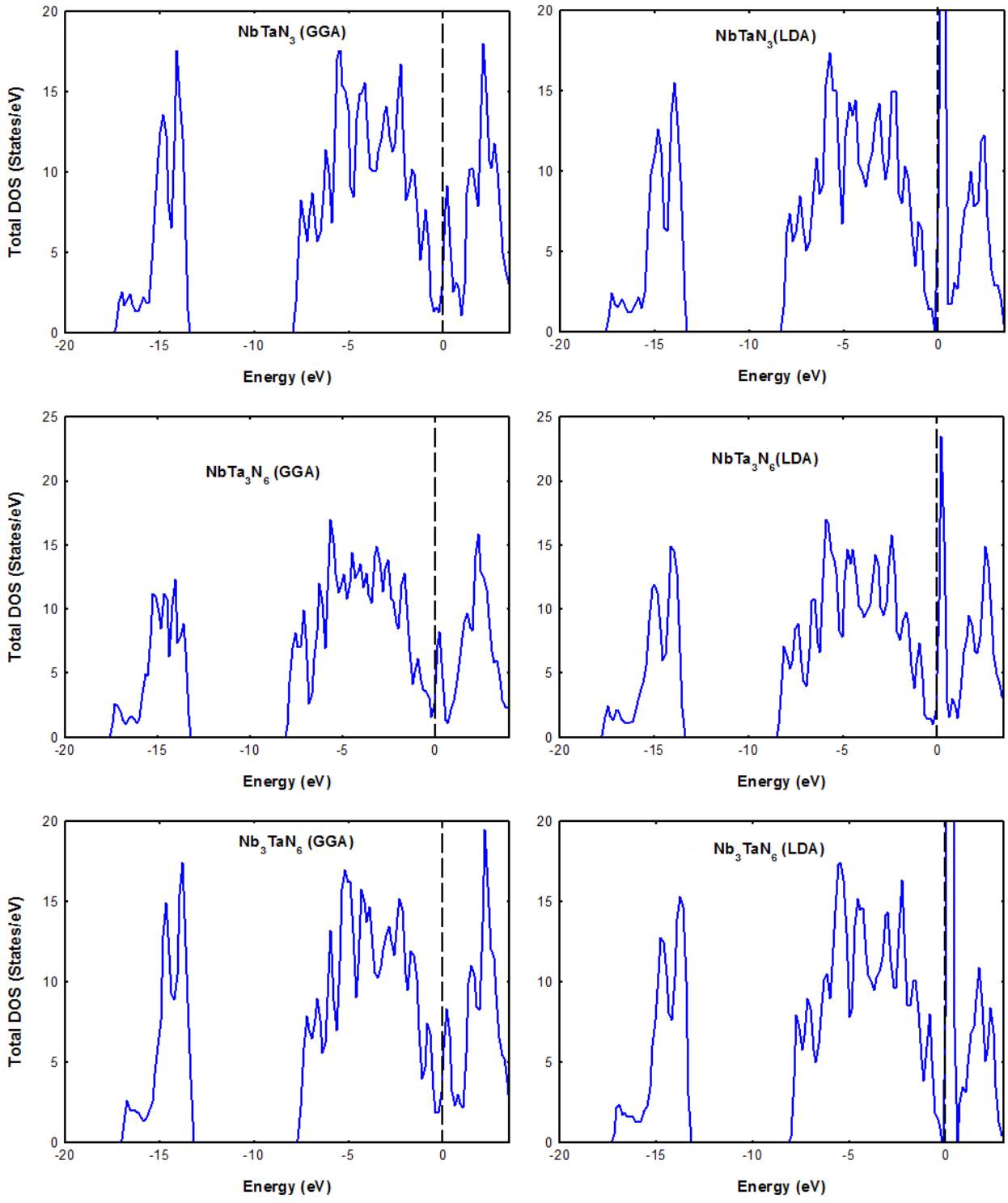
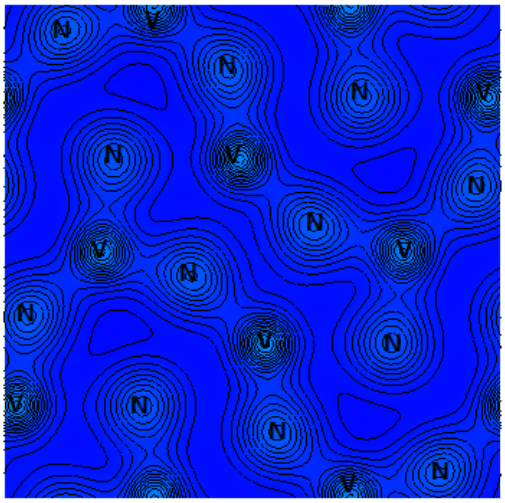
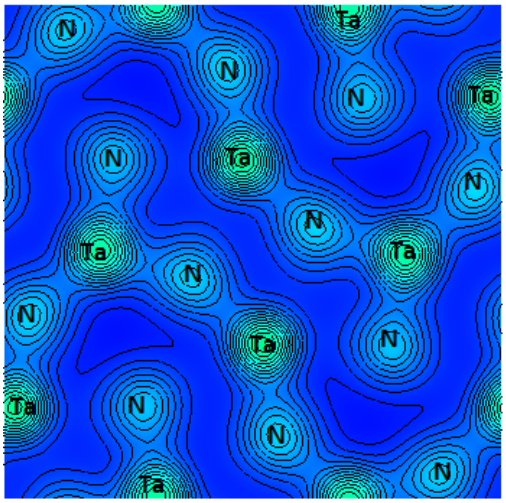


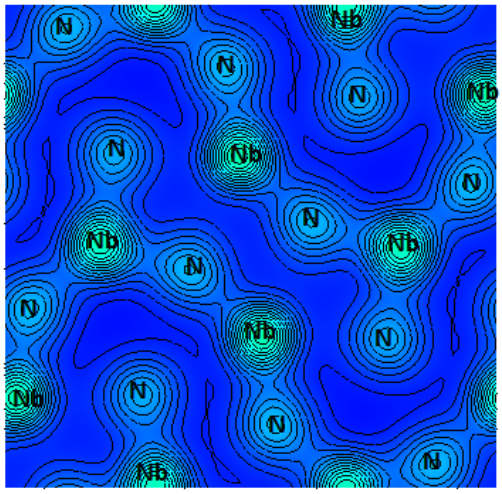
Figure 5.14: The plots of the total density of states of the ternary phases of the metal nitrides. The Fermi level is set at 0 eV and is indicated as a dashline.



(a) V_2N_3

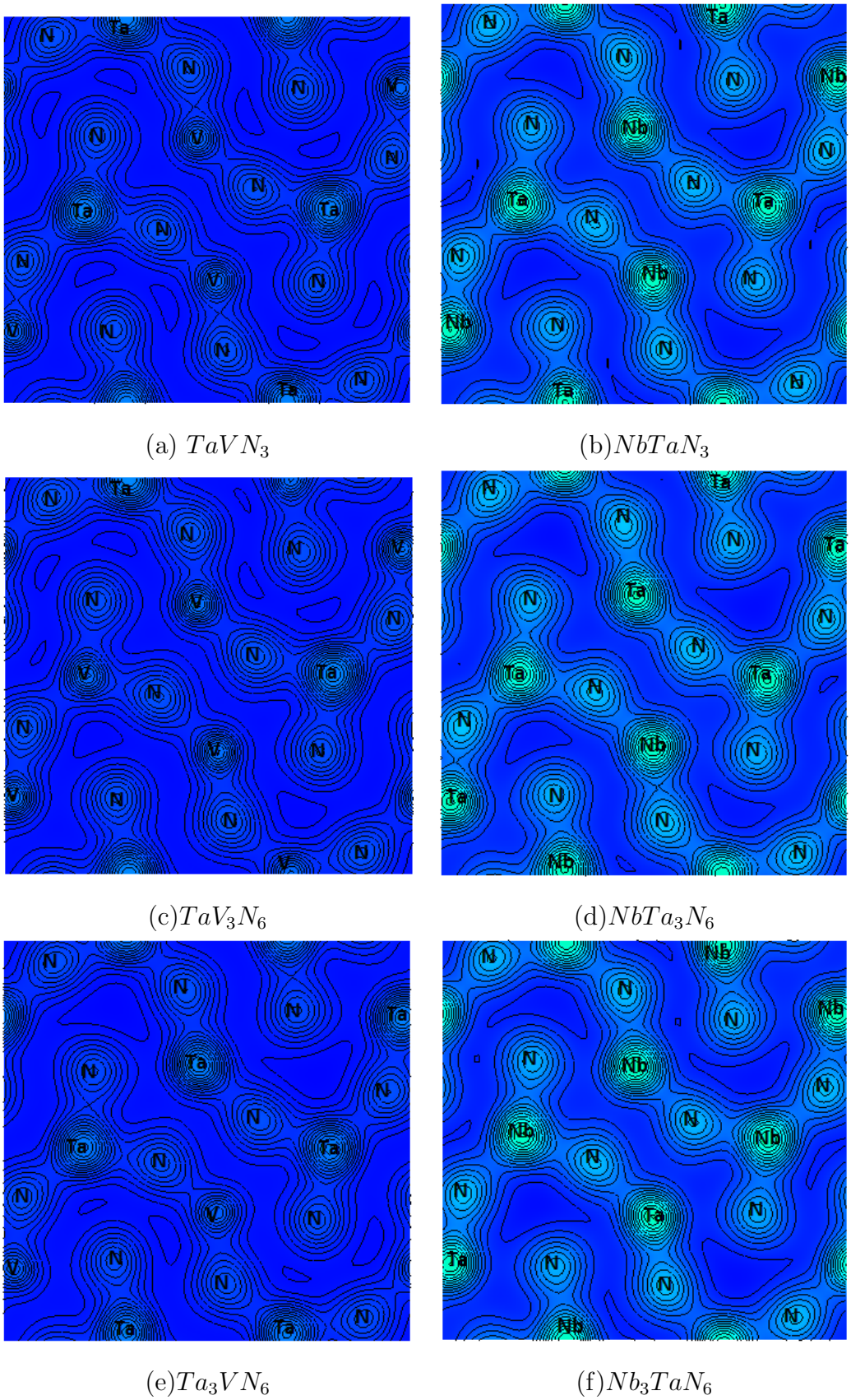


(b)Ta_2N_3



(c)Nb_2N_3

Figure 5.15: The plots of the charge density distributions of the binary metal nitrides in the 001 plane.



(a) $TaVN_3$ (b)$NbTaN_3$

(c)TaV_3N_6 (d)$NbTa_3N_6$

(e)Ta_3VN_6 (f)Nb_3TaN_6

Figure 5.16: The plots of the charge density distributions of the ternary metal nitrides in the 001 plane.

6. Conclusion

In this work, we have applied ab-initio calculations to investigate physical and electronic properties of the orthorhombic metal nitrides of tantalum, vanadium and niobium. The primary goal of this theoretical work is to discover new ultrahard materials. We have presented explicitly the calculated cell geometries, the elastic constants, the effective Voigt isotropic moduli, the equilibrium of state properties of the bulk modulus, the relative stability and the electronic properties at zero pressure and temperature for the advanced metal nitrides M_2N_3 (where M=Ta, V, Nb) and their ternary phases, using LDA and GGA within the plane-wave pseudopotential density functional theory. The results we obtained from the calculation of the optimized cell geometry of Ta_2N_3 were in good agreement with the experimental results of Zerr *et al.*[6] and the recent theoretical work of Jiang *et al.*[7]. We found the calculated lattice parameters were 1% larger than the experimental values.

From the GGA calculations, a negative value of one of the elastic constants (the C_{44} value) of Ta_2N_3 was found. The negative elastic constant implies that it can easily deform in that direction on the application of a high external force. This is contrary to the Born criteria [67] and suggests that the material is not stable. However, the corresponding LDA is positive and therefore not in agreement with this, so we suggest that no conclusion can be drawn regarding the stability of Ta_2N_3. One point however is that the elastic moduli of Ta_2N_3, V_2N_3 and Nb_2N_3, obtained using both the LDA and GGA functionals, are high. The calculated bulk moduli range between 291 and 413 GPa, a shear moduli between 133 and 218 GPa, and the Young's moduli between 353 and 553 GPa. These moduli are indicative of potentially good candidates for ultrahard materials. On the whole, the LDA calculations of Ta_2N_3, V_2N_3 and Nb_2N_3 predict higher elastic moduli as well as a smaller cell volumes than those obtained using the GGA. This is typical of the GGA calculation which are expected to underestimate the elastic moduli [77]

The effect of addition of vanadium (V) or niobium (Nb) to Ta_2N_3 was studied using both

in the LDA and the GGA calculations. These calculations yielded positive values of C_{44} and indicates enhance the stability of the ternary phases. This was observed almost in all the ternary phases using both the LDA and GGA functional. The one exception was TaV_3N_6 where the GGA predicted negative value of C_{44} while LDA yielded a positive value. It is, however, not possible to say conclusively whether TaV_3N_6 is unstable or not. The predicted bulk moduli for the ternary phases range between 306 and 405 GPa. A large shear modulus which represent a large resistance to plastic deformation is an absolute requisite for any new ultrahard material we are seeking. From our calculations of the shear modulus (using both the LDA and the GGA functionals) are fairly high because of the relatively high Poisson's ratio, which represents the stability of a crystal against shear. Our predicted values of the shear modulus for the ternary phases range between 118 and 227 GPa, with a Young's modulus between 314 and 573. The elastic properties of the ternary phases have shown that addition of a low concentration of vanadium or niobium to Ta_2N_3 can result in very promising improvements in hardness. Therefore, in the absence of experimental data, we suggest that the ternary phases have increased hardness compared to Ta_2N_3.

The experimental values of the isotropic properties of diamond are: $B = 442$ GPa, $G = 544$ GPa, $Y = 1142$ GPa and $\nu = 0.1$ [71]. Our prediction for the bulk and the shear moduli are in the range of 30-60% lower than the corresponding values for diamond. It is worth noting that there is a considerably good agreement between the isotropic bulk modulus obtained from the elastic constants with that obtained via the fit to the first order Birch equation of state B_0. The electronic structure calculation shows that the advanced metal nitrides and their ternary phases are all metallic because of their finite density of states at the Fermi energy level E_f.

6.1 Direction for Future Work

The advanced metal nitrides systems, during the course of this work have shown that they can be considered as important materials. Therefore, they are open for future research work. It would be quite interesting to carry out optimization calculation for the ternary phase - TaV_3N_6 under different other plane wave energy cutoffs. This is to establish good convergence of the system and to compare with findings of this study. It may also be possible to perform calculations on the advanced metal nitrides system at finite temperature and pressure using the Car - Parrinello molecular dynamics with variable unit cell parameters.

References

[1] M. L. Cohen. *Science*, 26:Pg 307, (1993).

[2] M. L. Cohen. *Science*, 234:Pg 549, (1986).

[3] E. Fermi. *Nuovo Cimente*, 11:Pg 157, (1934).

[4] P. E. Blöchl, O. Jepsen, and O. K. Andersen. *Physical Review B*, 49:Pg 16223, (1947).

[5] G. Kresse and D. P. Joubert. *Physical Review B*, 59:Pg 1758, (1999).

[6] A. Zerr, G. Miehe, J. Li, D. A. Dzivenko, V. K. Bulatov, H. Höfer, N. Bolfan-Casanova, M. Fialin, G. Brey, T. Watanabe, and M. A. Yoshimura. *Advanced Functional Material*, 19:Pg 2282, (2009).

[7] C. Jiang, Z. Lin, and Y. Zhao. *Physical Review Letters*, 103:Pg 185501, (2009).

[8] A. Y. Ganin, L. Kienle, and G. V. Vajenine. *European Journal of Inorganic Chemistry*, page Pg 3233, (2004).

[9] C. Ravi. *Computer Coupling of Phase Diagram and Thermochemistry*, 33:Pg 467, (2009).

[10] E. I. Isaev, S. I. Simark, I. A. Abrikosov, R. Ahuja, Y. K. vekilov, M. I. Katsnelson, A. I. Lichtenstein, and B. Johansson. *Journal of Applied Physics*, 101:Pg 123519, (2007).

[11] M. C. Payne, M. P. Teter, D. C. Allan, T. A. Arias, and J. D. Joannopoulos. *Reviews of Modern Physics*, 64(4):Pg 1045, (1992).

[12] G. Kresse, M. Marsman, and J. Furthmüller. *Vienna Ab-intio Simulation Package*. Computational Physics, Faculty of Physics, Universität Wien, Sensengasse 8, A-1130 Wien, Austria, (2009).

[13] J. Haines, J. M. Leger, and G. Bocquillon. *Annual Review of Materials Research*, 31:Pg 1, (2001).

[14] V. V. Brazhkin, A. G. Lyapin, and R. J. Hemley. *Philosophical Magazine A*, 82:Pg 231, (2002).

[15] R. B. Kaner, J. J. Gilman, and S. H. Tolbert. *Science*, 308:Pg 1268, (2005).

[16] F. Gao, J. He, E. Wu, S. Liu, D. Yu, D. Li, S. Zhang, and Y. Tian. *Physical Review Letters*, 91:Pg 015502–1, (2003).

[17] R. Riedel. *Advanced Materials*, 6:Pg 549, (1994).

[18] F. M. Mmethi. An Ab-initio Computional Investigation into the Properties of Potentially Ultra-hard Metal Oxynitrides. Msc, University of Witwatersrand, (2008).

[19] M. L. Cohen. *Annual Reviews of Materials Science*, 30:Pg 1, (2000).

[20] Y. P. Lu and D. W. He. *Journal of Applied Physics*, 105:Pg 083540, (2009).

[21] S. D. Mo, L. Ouyang, W. Y. Ching, I. Tanaka, Y. Koyama, and R. Riedel. *Physical Review Letters*, 83:Pg 5046, (1999).

[22] A. Zerr, G. Miehe, G. Serghiou, M. Schwarz, E. Kroke, R. Riedel, H. Fueb, P. Kroll, and R. Boehler. *Nature London*, 400:Pg 340, (1999).

[23] R. Riedel. *Handbook of Ceramic Hard Materials*. Wiley-VcH Verlag GmbH, D-69469 Weinhein (Federal Republic of Germany), (2000).

[24] M. Hebbache. *Solid State Communication*, 113:Pg 427, (2000).

[25] W. R. Matizamhnka. Development of a Potential Hard $Ta_{1-x}Zr_{1+x}O_{1+x}N_{1-x}$ Material. Msc, University of Witwatersrand, (2007).

[26] J. J. Gilman, R. W. Cumberland, and R. B. Kaner. *International Journal of Refactory Metal and Hard Materials*, 24:Pg 1, (2006).

[27] W. Kohn. *Reviews of Modern Physics*, 71(5):Pg 1253, (1999).

[28] L. H. Thomas. *Proceedings of Cambridge Philosophical Society*, 23:Pg 542, (1927).

[29] R. M. Martin. *Electronic Structure; Basic Theory and Practical Methods*. Cambridge University Press, (2004).

[30] J. Simons. *An Introduction of Theoretical Chemistry*. Cambridge University Press, (2003).

[31] P. Hohenberg and W. Kohn. *Physical Review*, 136(3B):B864, (1964).

[32] W. Kohn and L. J. Sham. *Physical Review*, 140(4A):Pg 1133, (1965).

[33] J. C. Slater. *Physical Review B*, 18(12):Pg 7165, (1978).

[34] J. P. Perdew, J. A. Chevary, S. H.Vosko, K. A. Jackson, M. R. Pederson, D. J. Singh, and C. Fiolhais. *Physical Review B*, 46:Pg 6671, (1992).

[35] J. P. Perdew and A. Zunger. *Physical Review B*, 23:Pg 5048, (1981).

[36] D. M. Ceperley and B. J. Alder. *Physical Review Letters*, 45:Pg 566, (1980).

[37] J. P. Perdew, K. Burke, and M. Ernzerhof. *Physical Review Letters*, 77(18):Pg 3865, (1996).

[38] J. Hafner. *Journal of Computational Chemistry*, 29:Pg 2044, (2008).

[39] R. P. Feynman. *Physical Review B*, 38:Pg 340, (1939).

[40] B. Meyer. *Computational Nanoscience*, 31:Pg 71, (2006).

[41] N. W. Ashcroft and N. D. Mermin. *Solid State Physics*. Saunders College Publishing, Philadelphia, (1976).

[42] V. Mofokeng. Transition Metal Carbides and Nitrides: Numerical Simulation of Properties and Trend. Msc, University of Witwatersrand, (2003).

[43] J. K. Dewhurst. *Computer Modelling of Superhard Metal Dioxide*. Phd, Witwatersrand University, (1999).

[44] D. J. Chadi and M. L. Cohen. *Physical Review B*, 8:Pg 5747, (1973).

[45] H. J. Monkhorst and J. D. Pack. *Physical Review B*, 13:Pg 5188, (1976).

[46] J. Moreno and J. M. Soler. *Physical Review B*, 45:Pg 13891, (1992).

[47] J. C. Phillips and L. Kleinman. *Physical Review*, 116:Pg 287, (1959).

[48] N. Troullier and J. L. Martins. *Physical Review B*, 43:Pg 1993, (1991).

[49] D. R. Hamann, M. Schlüter, and C. Chiang. *Physical Review Letters*, 43:Pg 1494, (1979).

[50] P. E. Blöchl. *Physical Review B*, 50:Pg 17953, (1994).

[51] M. Marsman and G. Kresse. *Journal of Chemical Physics*, 125:Pg 104101, (2006).

[52] B. Mazumder and A. L. Hector. *Journal of Material Chemistry*, 18:Pg 1392, (2008).

[53] R. B. Kaner, J. J. Gilman, and S. H. Tolbert. *Science*, 308:Pg 1268, (2006).

[54] H. Y. Chung, M. B. Weinberger, J. B. Levine, A. kavener, J. M. Yang, S. H. Tolbert, and R. B. Karner. *Science*, 316:Pg 436, (2007).

[55] A. Zerr, G. Miehe, and R. Riedel. *Nature Materials*, 2:Pg 185, (2003).

[56] P. Kroll, T. Schröter, and M. Peters. *Angewandte Chemie International Edition*, 44:Pg 4249, (2005).

[57] S. J. Henderson and A. L. Hector. *Solid State Chemistry*, 179(3B):Pg 3518, (2006).

[58] J. C. Crowhurst, A. F. Goncharov, B. Sadigh, C. L. Evans, P. G. Morrall, J. L. Ferreira, and A. G. Nelson. *Science*, 311:Pg 1275, (2006).

[59] A. F. Young, C. Sanloup, E. Gregoryanz, S. Scandolo, R. J. Hemley, and H. K. Mao. *Physical Review Letters*, 96:Pg 155501, (2006).

[60] J. Z. Jiang, F. Kragh, D. J. Frost, K. Stahl, and H. Lindelov. *Journal of Physical Condensed Matter*, 13:L515, (2001).

[61] A. Zerr, M. Kemfe, M. Schwarz, E. Kroke, M. Göken, and R. Riedel. *Journal of American Ceramic Society*, 85:Pg 85, (2002).

[62] C. M. Fang, E. Orhan, G. A. de Wijs, H. T. Hintzen, R. A. de Groot, R. Marchand, J.-Y. Saillardd, and G. de With. *Journal of Material Chemistry*, 11:Pg 1248, (2001).

[63] N. E. Brese and M. O'keeffe. *Acta Crystallography*, 47(Sect. C):Pg 2291, (1991).

[64] J. F. Nye. *Physical Properties of Crystals: Their Representation by tensors and Matrices*. Oxford University Press, New York, ISBN 0198511655, (1985).

[65] P. Ravindran, J. Wills, and O. Eriksson. *Journal of Applied Physics*, 84(9):Pg 4891, (1998).

[66] Y. Lee. *First Principle Calculations for X-ray Resonant Spectra and Elastic Properties*. Phd, Iowa State University, (2004).

[67] M. Born and K. Hung. *Dynamical Theory of Crystal Lattices*. Clarendon, Oxford, (1956).

[68] M. Mattesini and S. F. Matar. *Physical Review B*, 65:Pg 075110, (2001).

[69] R. Hill. *Proceedings of the Physics Society London*, 65:Pg 349, (1952).

[70] S. F. Pugh. *Philosophical Magazine*, 45:Pg 823, (1954).

[71] J. E. Lowther. *Physical Review B*, 73:Pg 134110, (2006).

[72] F. D. Murnaghan. *Proceedings of the National Academy of Sciences*, 30:Pg 8244, (1944).

[73] F. Birch. *Journal of Geophysical Research*, 57:Pg 227, (1952).

[74] P. Vinet, J. H. Rose, J. Ferrante, and J. R. Smith. *Journal of Physical Condensed Matter*, 1:Pg 1941, (1989).

[75] F. Birch. *Physical Review*, 71(11):Pg 809, (1947).

[76] J. P. Perdew, K. Burke, and M. Ernzerhof. *Physical Review Letters*, 77:Pg 3865, (1996).

[77] C. Filippi, D. J. Singh, and C. J. Umrigar. *Pyhsical Review B*, 50:Pg 14947, (1994).

[78] R. E. Watson and M. Weinert. *Solid State Physics: Transition-Metal and their Alloys*. Academic Press, (2001).

[79] O. Bisi, C. Calandra, L. Braicovich, I. Abbati, G. Rossi, I. Lindau, and W. E. Spicer. *Journal of Physics C: Solid State Physics*, 15:Pg 4707, (1982).

[80] M. I. Aroyo, A. Kirov, C. Capillas, J. M. Perez-Mato, and H. Wondratschek. *Acta Crystallographica Section A*, 62(2):Pg 115, (2006).

[81] P. Blaha, K. Schwarz, G. K. H. Madsen, D. Kvasnicka, and J. Luitz. *WIEN2K, An Augmented Plane Wave + Local Orbitals Program for Calculating Crystal Properties*. K. Schwarz, (2001).

[82] Z. Wu and R. Cohen. *Pyhsical Review B*, 73:Pg 235116, (2006).

[83] V. L. Moruzzi, P. Oelhafen, and A. R. Williams. *Physical Review B*, 27:Pg 7194, (1983).

[84] M. H. Tsai, S. C. Sun, H. T. Chiu, C. E.Tsai, and S. H. Chuang. *Applied Physics Letter*, 67:Pg 1128, (1995).

[85] M. Jansen, H. P. Letschert, and D. Speer. *European Patent*, (Pg 592867), (1993).

[86] P. kroll. *Physical Review Letters*, 9(12):Pg 125501, (2003).

[87] T. Hong, T. J. Yang, X. Q. Guo, A. J. Freeman, T. Oguchi, and J. H. Xu. *Physical Review B*, 43:Pg 1940, (1991).